Physics of Plasmas ARTICLE scitation.org/journal/php

Continuum gyrokinetic simulations of edge plasmas in single-null geometries

Cite as: Phys. Plasmas **28**, 032508 (2021); doi: 10.1063/5.0039169
Submitted: 30 November 2020 · Accepted: 26 February 2021 ·
Published Online: 29 March 2021

M. Dorf[a] and M. Dorr

AFFILIATIONS

Lawrence Livermore National Laboratory, Livermore, California 94550, USA

Note: This paper is part of the Special Collection: Papers from the 62nd Annual Meeting of the APS Division of Plasma Physics.
[a]**Author to whom correspondence should be addressed:** dorf1@llnl.gov

ABSTRACT

The first continuum gyrokinetic calculations of electrostatic ion scale turbulence are presented for the case of a diverted tokamak geometry. The simulation model solves the long-wavelength limit of the full-F gyrokinetic equation for ion species coupled to the quasi-neutrality equation for electrostatic potential variations, where a fluid model is used for an electron response. In order to facilitate simulations of highly-anisotropic microturbulence in the presence of strong magnetic shear and a magnetic X-point, a numerical algorithm utilizing a locally field-aligned multiblock coordinate system has been developed and implemented in the 5D finite-volume code COGENT. In this approach, the toroidal direction is divided into blocks, such that within each block, the cells are field-aligned and a non-matching grid interface is allowed at block boundaries. The toroidal angle corresponds to the "coarse" field-aligned coordinate, whereas the poloidal cross section, comprised of the radial and poloidal directions, is finely gridded to resolve short-scale perpendicular turbulence structures and to support accurate re-mapping (interpolation) at block boundaries. The 5D simulations explore cross-separatrix ion scale turbulence in the presence of a self-consistent radial electric field and address the effects of magnetic-shear stabilization in the X-point region.

I. INTRODUCTION

The processes at the tokamak plasma edge play a crucial role for achieving a steady state burning fusion plasma, and it is important to develop an improved theoretical understanding of edge plasma transport. The problem, however, presents substantial challenges for analytical or numerical analysis due to (a) complex magnetic geometry, including both open and closed magnetic field lines **B**, (b) steep radial gradients comparable to ion drift-orbit excursions, and (c) a variation in the collision mean-free path along **B** from long to short compared to the magnetic connection length. A gyrokinetic equation that includes a detailed collision operator must be solved to capture these key features.

Presently, there are two main approaches to solving a kinetic (here, gyrokinetic) equation: (i) the particle-in-cell (PIC) method, which makes use of macroparticles to integrate along the characteristics of the kinetic equation, and (ii) the continuum method, in which the kinetic equation is discretized on a phase-space grid. The PIC approach provides an efficient computational tool to solve the high-dimensional kinetic equation and is well-suited for parallel programming. However, in contrast to a continuum discretization, it suffers from statistical particle noise and limited phase space density resolution. Both methods have been successfully utilized to study plasma 4D axisymmetric transport and 5D turbulence in a tokamak core. The two approaches complement each other, provide opportunities for cross-code verification, and stimulate progress in understanding physical properties of core plasmas.

Contrary to the beneficial co-existence of about a dozen PIC and continuum gyrokinetic codes for core plasmas,[1–7] the gyrokinetic modeling of a tokamak edge that includes the magnetic separatrix has been represented, to date, only by the PIC method. This is despite the fact that the particle noise issues become even more pronounced in the edge. Indeed, due to generally small deviations from an *a priori* known local Maxwellian background in a core region, a so-called delta-F approach can be utilized, which mitigates the statistical noise level in core PIC simulations as N^{-1}, where N is the number of macroparticles. In contrast, the presence of a steep gradient region in the edge of a tokamak, for example, under H-mode conditions, can lead to pronounced deviations of a background ion distribution function from a local Maxwellian. Therefore, gyrokinetic edge codes should include modeling of the background quasi-equilibrium dynamics, that is, a full-F approach is required. In this case, the noise-to-signal ratio decreases only as $\sqrt{N^{-1}}$, and simulations of low-amplitude turbulence

subject to adequate representation of the background dynamics can require a very large number of macroparticles.[8]

Although PIC simulations of edge plasmas suffer from the enhanced particle noise problem, extension of underlying numerical algorithms from the core to the edge region has been substantially more straightforward for PIC than for continuum methods. One central feature of a continuum simulation model that poses a significant challenge is the presence of the magnetic separatrix within the simulation domain. In order to facilitate simulations of highly anisotropic plasma transport and turbulence, the spatial grids are typically chosen to be aligned with the magnetic flux surfaces (for axisymmetric transport studies) or magnetic field lines (for 5D turbulence studies). However, such coordinate surfaces have diverging metric coefficients at the X-point of the magnetic separatrix, thereby introducing a challenge for high-order accurate discretization methods. In contrast to the continuum approach, PIC methods use macroparticles to integrate along the characteristic of a kinetic equation, and therefore are much less sensitive to the presence of the X-point, where a particle's gyrocenter velocity is well defined.

While the PIC method has been extensively used in the past decade for gyrokinetic modeling of the tokamak edge,[9] significant advances have been recently made in developing a continuum approach for modeling fusion plasmas in complex magnetic geometries that can include an X-point.[10] The corresponding numerical methods have been developed and implemented in the finite-volume Eulerian code COGENT (COntinuum Gyrokinetic Edge New Technology). A distinguishing feature of the COGENT approach is the use of a multiblock grid technology,[11] in which logically distinct blocks are smoothly mapped from rectangular computational domains and a high-order interpolation is used to provide inter-block coupling. For the case of a single-null magnetic geometry, the blocks describe different parts of the computational domain, such as core, scrape-off-layer (SOL), and private flux (PF) regions. While the present paper reports on the results of cross-separatrix simulations performed with the COGENT code, it is worthwhile to note other ongoing efforts in the continuum gyrokinetic modeling of a tokamak edge that make use of the Gkeyll[12] and GENE[13] codes. These studies, however, are presently limited to the open field line region (e.g., SOL).

The COGENT code solves full-F gyrokinetic equations in the long-wavelength electrostatic limit for an arbitrary number of plasma species. A succession of increasingly detailed collision models is available and includes linearized[14] and fully nonlinear Fokker-Planck[15] collision operators. The code has been previously applied to the analysis of 4D axisymmetric transport in annular[14,16] and single-null[17,18] geometries and to the modeling of the ion temperature gradient (ITG) instability in a toroidal annulus geometry.[19] The present work extends the range of COGENT applications to the analysis of ion-scale turbulence in a single-null geometry. Self-consistent variations of an electrostatic potential are obtained by making use of the quasi-neutrality equation, $\nabla \cdot \mathbf{j} = 0$, coupled to a simple isothermal electron fluid response. The results of COGENT simulations elucidate the stabilizing role of edge radial electric fields and enhanced magnetic shear in the X-point region. To our knowledge, these are the first continuum gyrokinetic simulations of cross-separatrix plasma turbulence.

In order to facilitate simulations of highly-anisotropic microturbulence in the presence of strong magnetic shear and a magnetic X-point, a numerical algorithm utilizing a locally field-aligned multiblock coordinate system has been developed. In this approach, the toroidal direction is divided into blocks, such that within each block, the cells are field-aligned and a non-matching (non-conformal) grid interface is allowed at block boundaries. The toroidal angle corresponds to the "coarse" field-aligned coordinate, whereas the poloidal cross section, comprised of the radial and poloidal directions, is finely gridded to resolve short-scale perpendicular turbulence structures and to support accurate re-mapping (interpolation) at block boundaries. We note that such a numerical scheme shares certain features of the so-called flux coordinate independent (FCI) approach used for Eulerian fluid modeling in X-point geometries.[20] In particular, the FCI method also employs coarse toroidal discretization and computes large-scale parallel gradients by interpolating data in finely gridded poloidal planes. However, in contrast to the FCI method, the magnetic flux surfaces are retained here as coordinate surfaces to minimize numerical pollution errors; furthermore, the COGENT implementation makes use of a systematic finite-volume discretization. It is also instructive to note that field-aligned interpolation techniques, which allow the minimization of the number of spatial points required to represent fluctuation quantities, have been also adopted in the semi-Lagrangian gyrokinetic simulations in core, i.e., closed-field-line, geometries.[21–23]

This paper is organized as follows. The simulation model and its numerical implementation are described in Secs. II and III, respectively. Section IV presents the results of verification studies performed in simplified annular and slab geometries. The results of turbulence simulations in a single-null geometry are discussed in Sec. V. Finally, the conclusions of the present work are summarized in Sec. VI.

II. SIMULATION MODEL

A. Gyrokinetic equation

The simulation model adopted in this work solves the long-wavelength limit of a gyrokinetic equation for a gyrocenter ion distribution function $f_i(\mathbf{R}, \mathrm{v}_\parallel, \mu)$ given by

$$\frac{\partial (B_\parallel^* f_i)}{\partial t} + \nabla \cdot \left(\dot{\mathbf{R}} B_\parallel^* f_i \right) + \frac{\partial}{\partial \mathrm{v}_\parallel} \left(\dot{\mathrm{v}}_\parallel B_\parallel^* f_i \right) = C\left[B_\parallel^* f_i \right]. \tag{1}$$

Here, $\mathbf{R}$ is the gyrocenter coordinate, ∇ is the gradient with respect to $\mathbf{R}$, and the gyrocenter velocity $\dot{\mathbf{R}}$ is given by

$$\dot{\mathbf{R}} = \frac{1}{B_\parallel^*} \left[\mathrm{v}_\parallel \mathbf{B}^* + \frac{c}{Z_i e} \mathbf{b} \times (Z_i e \nabla \Phi + \mu \nabla B) \right]. \tag{2}$$

The evolution of the gyrocenter parallel velocity is specified by

$$\dot{\mathrm{v}}_\parallel = -\frac{1}{m_i B_\parallel^*} \mathbf{B}^* \cdot (Z_i e \nabla \Phi + \mu \nabla B), \tag{3}$$

where m_i and Z_i are the ion species mass and charge state, respectively, e is the electron charge, c is the speed of light, $\mathbf{B} = B \cdot \mathbf{b}$ is the magnetic field with $\mathbf{b}$ denoting the unit vector along the field, $\mathbf{B}^*(\mathbf{R}, \mathrm{v}_\parallel) \equiv \mathbf{B} + (c m_i / Z_i e) \mathrm{v}_\parallel \nabla \times \mathbf{b}$, $B_\parallel^* = \mathbf{B}^* \cdot \mathbf{b}$, and the long-wavelength limit, $k_\perp \rho_i \ll 1$, is presently adopted for electrostatic potential variations, $\Phi(\mathbf{R}, t)$, and collision models, $C[B_\parallel^* f_i]$. Here, $\rho_i = V_{Ti}/\Omega_i$ is the particle thermal gyroradius, $V_{Ti} = \sqrt{T_i/m_i}$ is the thermal velocity, $\Omega_i = Z_i e B/(m_i c)$ is the cyclotron frequency, and $k_\perp^{-1}$ represents the

characteristic length-scale for variations in the electrostatic potential and distribution function perturbations.

B. E-field models: Gyrokinetic Poisson model

Two models for self-consistent variations of an electrostatic potential are used in this work. The first option utilizes the long-wavelength limit of the gyrokinetic Poisson equation:

$$\nabla_\perp \cdot \left(\frac{c^2 m_i n_i}{B^2} \nabla_\perp \Phi \right) = e(n_e - Z_i n_i), \tag{4}$$

coupled to the linearized adiabatic electron response,

$$n_e = Z_i \langle n_{i0} \rangle (1 + e\Phi/T_e - e\langle \Phi \rangle / T_e). \tag{5}$$

Here, T_e is the electron temperature, which is assumed to be a constant on flux surfaces, $\nabla_\perp \equiv \nabla - \mathbf{b}(\mathbf{b}\cdot\nabla)$ is the perpendicular gradient operator, $\langle Q \rangle$ is the flux-surface average defined as the volume average of Q between two neighboring flux surfaces, ψ and $\psi + d\psi$, and the ion gyrocenter density is specified by

$$n_i = \frac{2\pi}{m_i} \int f_i B_\parallel^* dv_\parallel d\mu. \tag{6}$$

Note that "pressure-term" corrections in the gyroaveraged gyrocenter ion density, $\delta n_i \sim \nabla_\perp^2 (n_i V_{Ti}^2)/\Omega_i^2$, are neglected in Eq. (4) as they are small in the long-wavelength limit. Finally, $\langle n_{i0} \rangle$ corresponds to the flux surface average of the initial ion gyrocenter density.

The reduced electron adiabatic model in Eq. (5) has been successfully used for decades in core plasma gyrokinetic simulations of slow, ion timescale, processes, $\omega \ll k_\parallel V_{Te}$, such as 5D ITG turbulence and 4D neoclassical transport. This model, however, cannot be straightforwardly extended to simulations that span the magnetic separatrix. From the physical point of view, Eq. (5) manifests a constant-in-time flux surface average of the electron density, $\partial \langle n_e \rangle / \partial t \equiv 0$, which, on closed flux surfaces, is equivalent to the zero-flux surface average of the electron radial particle flux. While the condition, $\partial \langle n_e \rangle / \partial t \equiv 0$, is approximately valid in a core region, such constraint is not applicable to the SOL plasmas due to the presence of large electron parallel losses to divertor plates. From the mathematical point of view, one can also note that the flux surface average operator acting on the potential perturbations $\langle \Phi \rangle$ [in Eq. (5)] is discontinuous across the separatrix.

C. E-field models: Vorticity model

In order to make use of reduced electron models in simulations that span the magnetic separatrix, a second option for self-consistent potential perturbations has been developed in COGENT based upon the quasi-neutrality ($\nabla \cdot \mathbf{j} = 0$) equation, written for the vorticity variable

$$\varpi = \nabla_\perp \cdot \left(\frac{c^2 n_i m_i}{B^2} \nabla_\perp \Phi \right). \tag{7}$$

Taking the partial time derivative of Eq. (4) and making use of Eq. (1), we obtain

$$\frac{\partial \varpi}{\partial t} = \nabla \cdot \mathbf{j}_e + \nabla \cdot \mathbf{j}_i. \tag{8}$$

Here, the ion gyrocenter current density is given by $\mathbf{j}_i = (2\pi Z_i e/m_i) \int \dot{\mathbf{R}} f_i B_\parallel^* dv_\parallel d\mu$, and the electron current density, $\mathbf{j}_e = -e\mathbf{V}_e n_e$, is obtained as follows. Assuming an isotropic electron fluid model, the perpendicular electron current density is given to the lowest order in the ratio of the electron gyroradius to the length scale of background plasma variations, ρ_e/L, by

$$\mathbf{j}_{\perp,e} = -\frac{c}{B} \nabla_\perp p_e \times \mathbf{b} + e n_e \frac{c}{B} \nabla_\perp \Phi \times \mathbf{b}, \tag{9}$$

where $p_e = n_e T_e$ is the electron pressure. Furthermore, adopting the collisional electron response in the parallel direction and neglecting small electron inertia, it follows that

$$j_\parallel = \sigma_\parallel \left(\frac{1}{e n_e} \nabla_\parallel P_e - \nabla_\parallel \Phi + \frac{0.71}{e} \nabla_\parallel T_e \right), \tag{10}$$

where $j_\parallel = e n_e (V_{\parallel,i} - V_{\parallel,e}) = e Z_i n_i V_{\parallel,i} + \varpi V_{\parallel,i} - e n_e V_{\parallel,e}$ is the parallel current density,

$$\sigma_\parallel = 1.96 n_e e^2 \frac{\tau_e}{m_e}, \tag{11}$$

is the parallel electron conductivity, and τ_e is the basic electron collisional term given by Braginskii.[24] Considering the lowest-order approximation for the ion parallel macroscopic velocity, $n_i V_{\parallel,i} = (2\pi/m_i) \int v_\parallel f_i B_\parallel^* dv_\parallel d\mu$ and combining Eqs. (8)–(10), we obtain

$$\frac{\partial \varpi}{\partial t} + \nabla \cdot \left(c \frac{-\nabla_\perp \Phi \times \mathbf{b}}{B} \varpi \right) + \nabla \cdot \left(\mathbf{b} V_{\parallel,i} \varpi \right) = B \nabla_\parallel \frac{j_\parallel}{B} + \nabla \cdot \left(\frac{2\pi Z_i e}{m_i} \int \mathbf{v}_\perp^m f_i B_\parallel^* dv_\parallel d\mu - \frac{c}{B} \nabla_\perp p_e \times \mathbf{b} \right). \tag{12}$$

Here, $\mathbf{v}_\perp^m \equiv \dot{\mathbf{R}}_\perp (\Phi = 0)$ is the magnetic drift velocity corresponding to the perpendicular component of the guiding center velocity in Eq. (2) for the case of a zero potential. We also note that in deriving the Reynolds stress term [the second term on the LHS of Eq. (12)], we neglected a small difference between B and $B_\parallel^*$.

The quasi-neutrality model in Eq. (12) appears similar to vorticity models adopted in drift-reduced fluid simulations (see, for instance, Ref. 25); however, it employs the ion gyrokinetic equation to evaluate the perpendicular ion current, and therefore retains important kinetic ion effects such as prompt X-point losses. We also note that the expression for vorticity in Eq. (7) omits the pressure term (often retained in fluid models) as a result of our assumptions underlying the long-wavelength limit of the gyrokinetic Poisson equation [Eq. (4)]. The long-wavelength limit may be of limited validity for describing edge plasma turbulence. Furthermore, we refer the reader to the analysis in Refs. 26–28 that address general applicability of the standard quasi-neutrality approach (as adopted in the gyrokinetic Poisson and vorticity models) for evaluating a long-wavelength radial electric field. While improving the electric field model will be the subject of our future studies, the primary purpose of this work is to analyze the performance of the underlying numerical algorithms with a simplified model that, however, captures edge-relevant instabilities such as ITG and resistive drift and ballooning modes. In the same manner, we further arbitrarily simplify the vorticity model in Eq. (12) by neglecting the parallel advection term and by replacing n_e with $Z_i n_i$ (i.e., neglecting the polarization density corrections) as follows:

$$\frac{\partial \varpi}{\partial t}+\nabla\cdot\left(c\frac{-\nabla_\perp\Phi\times\mathbf{b}}{B}\varpi\right)$$
$$=\nabla\cdot\left(\frac{2\pi Z_i e}{m_i}\int \mathbf{v}_\perp^m f_i B_\parallel^* dv_\parallel d\mu\right)+\nabla\cdot\left[\frac{cZ_i n_i T_e}{B}\left(\nabla\times\mathbf{b}+\frac{\mathbf{b}\times\nabla B}{B}\right)\right]$$
$$+B\nabla_\parallel\left[\frac{\sigma_\parallel}{B}\left(\frac{1}{eZ_i n_i}\nabla_\parallel(n_e T_e)-\nabla_\parallel\Phi+\frac{0.71}{e}\nabla_\parallel T_e\right)\right]. \quad (13)$$

We note that retaining polarization density corrections in the electron pressure on the last line of Eq. (13) was found to be important for the stabilization of high-$k\rho_i$ perturbations. Also, in deriving Eq. (13), we made use of the following identity:

$$\nabla\cdot\left(-\frac{\nabla_\perp p_e\times\mathbf{b}}{B}\right)=\nabla\cdot\left[\frac{p_e}{B}\left(\nabla\times\mathbf{b}+\frac{\mathbf{b}\times\nabla B}{B}\right)\right]. \quad (14)$$

Equation (13) represents the COGENT vorticity model for self-consistent variations of electrostatic potential that needs to be coupled with a model for an electron temperature. The present work adopts a simple isothermal electron model with $T_e = const$.

Finally, we note that both the gyrokinetic Poisson model in Eqs. (4) and (5) and the vorticity model in Eq. (13) should provide similar results in the ITG simulations for the case of a closed-flux-surface geometry and a hot (therefore, highly conductive) plasma. However, in contrast to the gyrokinetic Poisson model coupled to the adiabatic electron response, the vorticity model coupled to the fluid electron response can also adequately describe potential variations across the separatrix including the cooler (i.e., less conductive) open-field-lines outer-edge region and the corresponding effects of resistive drift and ballooning modes. These conclusions are confirmed in COGENT simulations presented in Sec. IV.

D. Boundary conditions

The phase-space advection operator in the ion gyrokinetic equation [Eq. (1)] requires specification of "inflow" fluxes at the phase-space boundaries. In the present studies, these fluxes are computed from the initial ion distribution. For instance, for the case of a local Maxwellian initialization, the boundary condition corresponds to the presence of a Maxwellian "bath" that maintains the initial boundary values of the density, parallel momentum, and temperature throughout the simulation.

Available radial boundary conditions for a potential include the standard Dirichlet and Neumann conditions as well as the following consistent condition that can be applied on the radial closed-flux-surface boundaries:

$$\left\langle\frac{c^2 n_i m_i}{B^2}|\nabla\psi|^2\right\rangle\frac{\partial\Phi}{\partial\psi}=\int_0^t dt\langle\nabla\psi\cdot\mathbf{j}_i\rangle. \quad (15)$$

The condition in Eq. (15) makes use of the quasi-neutrality equation [Eq. (8)], where a small contribution from the flux surface average of the radial electron current is neglected, and the potential, Φ, is assumed to be nearly constant on the boundary flux surface. Such a condition allows for consistent development of the long-wavelength background radial electric field at the radial boundaries, while plausibly mitigating near-boundary turbulence by suppressing short-wavelength poloidal variations in Φ. The use of the boundary condition in Eq. (15) can accommodate large plasma gradients at the radial boundaries as demonstrated in Sec. IV. This alleviates the need for radial buffer regions, which are typically included in continuum full-F gyrokinetic simulations that employ the standard, i.e., Dirichlet or Neumann, conditions and use the buffer zones to diffuse the profile gradients and damp the turbulence.[4,29,30]

The cross-separatrix simulations presented in this work adopt a simple zero Dirichlet boundary condition for a potential at the divertor plates, $\Phi_{BC}^{plate}=0$. It is, however, instructive to note that the vorticity model in Eq. (13) can be supplemented by the commonly used logical sheath boundary condition for the potential on the plasma side of the sheath (see, for instance, Ref. 31), $\Phi_{BC}^{plate}=-T_e/e\ln[2\sqrt{\pi}(j_\parallel-en_eV_{\parallel,i})/(en_eV_{Te})]+\Phi_p$, which will be described in a future publication. Here, the divertor plate is assumed to be conducting, and at a potential Φ_p, the effects of the perpendicular drift velocity are neglected, for simplicity.

III. NUMERICAL IMPLEMENTATION

A. Spatial discretization

COGENT employs high-order finite-volume methods to solve hyperbolic [Eq. (1)] and elliptic [Eq. (4)] equations on arbitrary spatial grids represented by logically distinct blocks that are smoothly mapped from rectangular computational domains.[10] Short-wavelength turbulence that determines transport properties of a tokamak plasma is distinguished by highly anisotropic perturbations, which are aligned with the magnetic field, and therefore motivate the use of a field-aligned coordinate system. However, the presence of the X-point and a strong magnetic shear in the edge of a diverted tokamak generate significant distortion of the control volumes if a globally field-aligned coordinate system is used. To deal with this issue, the following discretization concept has been adopted[19] (see Fig. 1).

The toroidal direction is divided into a number of blocks (wedges) such that a local coordinate system is field-aligned within a block. Furthermore, each toroidal block can consist of a number of sub-blocks employed to represent a single-null poloidal cross section as it is done in the 4D (axisymmetric) version of the code.[10,17,18] The grid is constructed by, first, creating a 2D (ψ,θ) mesh on a reference poloidal plane located in the middle of a toroidal block, and then by mapping it along the magnetic field lines. Here, ψ and θ denote the radial (e.g., flux-surface) and poloidal coordinates, respectively [see Fig. 1]. Assuming axisymmetric equilibrium magnetic geometry, the cell volumes can be constructed within each block in the same way. Due to the twist and shear of magnetic field lines, the grids in different blocks will not, in general, match at toroidal block interfaces. However, by increasing the number of toroidal blocks (thereby decreasing their size), the level of mismatch can be minimized even for large values of magnetic shear. In order to provide communication between the blocks, the grid in each block is smoothly extended along the field lines into the neighboring blocks, and such formed ghost-cells are filled by interpolating the corresponding valid-cell data. Due to the locally field-aligned nature of the discretization scheme, the number of degrees of freedom to describe short-wavelength turbulence remains optimal. That is, while a 2D grid in the poloidal cross section has to resolve fine-scale structures, e.g., $\lambda\sim\rho_i$, the toroidal direction, which corresponds to a field-aligned coordinate, can remain coarse as it only needs to resolve large-scale parallel structures.

The cross-separatrix simulations presented in this work adopt a magnetic flux surface coordinate, ψ, that spans the entire simulation

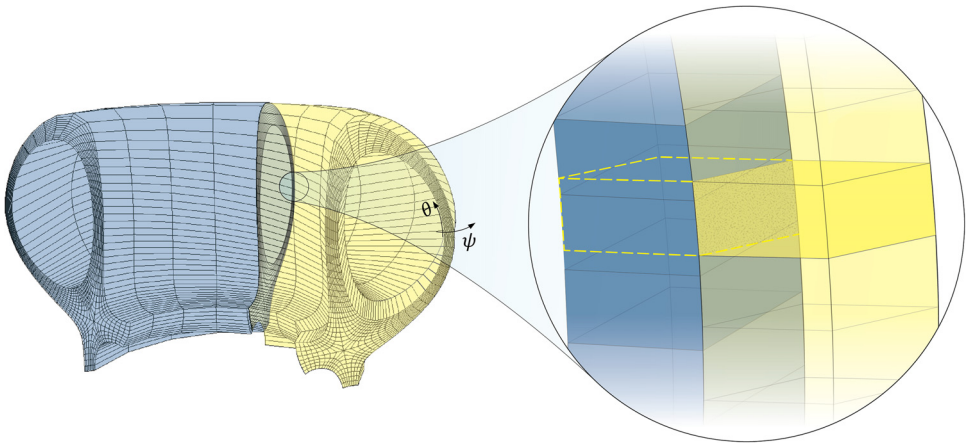

FIG. 1. Schematic of a locally field-aligned multiblock discretization scheme. The left panel shows a two-block structure with four toroidal valid cells in each block. Each toroidal block consists of eight poloidal sub-blocks that represent the global mapping in the poloidal (ψ, θ) plane. The poloidal plane block decomposition is not illustrated here and can be found elsewhere.[10] The right panel shows a zoom-in on the toroidal block interface. In order to compute fluxes on the cell face between the highlighted yellow cell and the corresponding ghost cell (shown with the yellow-dashed lines), data in the ghost cell have to be computed. The ghost cells are obtained by extending the field-aligned mapping into the ghost region, and since both toroidal blocks share the same flux-surface coordinate only 1D interpolation in the θ-direction is required. The three dark blue cells of the left block are used here for the quadratic interpolation.

domain including the X-point. Multiple sub-blocks are still used to discretize the poloidal plane as described in detail in Refs. 10, 17, 18; however, in contrast to the toroidal direction, the 2D (ψ, θ) grids in different poloidal sub-blocks are conformal and no interpolation is required to fill the corresponding poloidal and radial ghost cells. While such global use of the flux-surface coordinate reduces the order of convergence in the X-point region, it minimizes numerical pollution due to the presence of high electron parallel conductivity in the vorticity model. This pollution effect was reported in our earlier axisymmetric transport studies[18] and is discussed again in Secs. III C and IV D. For the cases where an electrostatic potential is fixed and the pollution effect is absent, global high-order convergence of the gyrokinetic equation was demonstrated with 4D COGENT simulations in a single-null geometry using controlled grid de-alignment in the X-point region.[10]

Due to the nonconformity of the toroidal cell faces at the shared block boundaries, special treatment of the inter-block interpolation and the evaluation of normal fluxes at the toroidal block boundaries are required to achieve conservative discretization. While the development of a high-order conservative 5D locally field-aligned COGENT is in progress, here we make use of a non-conservative second-order version, which can, nevertheless, test critical aspects of the numerical algorithms and provide insights into the physical properties of edge plasmas. This version utilizes a third-order upwind discretization of the gyrokinetic advection operator combined with a third-order [the truncation error of $O(h_\theta^3)$] interpolation scheme for the inter-block communication. Here, h_θ is the cell size in the θ-direction, in which 1D interpolation is performed.

It is instructive to note that our numerical scheme adopts the toroidal angle, ϕ, as a field-aligned coordinate (as employed here), in contrast to the poloidal angle, which is often adopted for the modeling of core[1] and edge[32] turbulence. The choice of the poloidal angle as a field-aligned coordinate can be more efficient for modeling of the processes characterized by a high toroidal mode number, where it is sufficient to simulate only a small part (wedge) of a full torus. On the other hand, the use of the toroidal angle as a field-aligned coordinate is more natural for near the X-point where it yields minimal twist of control volumes. It is further important to note the difference between the two approaches in the development of boundary conditions on axisymmetric divertor plates. For the case of a poloidal field-aligned coordinate, the divertor plates coincide with the poloidal boundary of the computational domain, which facilitates the implementation of the corresponding boundary conditions. However, for the case of the toroidal field-aligned coordinate, the plates are no longer conformal to the poloidal domain boundary, which has a "saw-tooth" shape in the plane $\psi = const$ as illustrated in Fig. 2. The divertor plates boundaries are presently handled by exploiting the long-wavelength nature of parallel variations in the potential and distribution function and by performing zero-order extrapolation of physical boundary conditions from the divertor plate onto the computational domain boundaries along magnetic field lines (see Fig. 2). For instance, a boundary

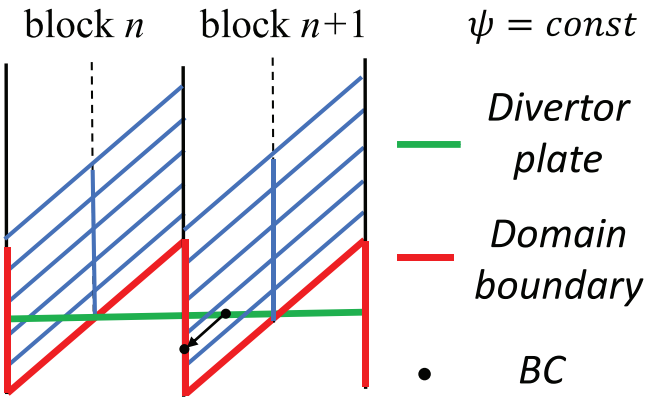

FIG. 2. Schematic of the divertor plate region ($\psi = const$ plane is shown). The physical boundary conditions on the straight-line divertor plate (green) are translated to the saw-tooth computational domain boundary (red).

condition, $\Phi_{BC}^{plate} = 0$, corresponding to conducting plates is applied to the computational domain boundary instead of the actual physical boundary. Improving such a low-order approach by making use of embedded boundary methods[33] is left to future work.

B. Gyrokinetic Poisson model implementation

In addition to the spatial discretization described above, developing an efficient approach to solving Eq. (4) is necessary. Although a variety of methods are available in COGENT to handle sparsely coupled elliptic equations, the presence of the flux-surface average potential in the RHS of Eq. (4), which governs the evolution of the axisymmetric (zonal-flow) component, introduces dense (long range, non-local) coupling. This problem is addressed in COGENT by performing "subspace" iterations, where we interchangeably solve for flux-surface averaged (zonal) and non-zonal components of Φ (which belong to orthogonal functional sub-spaces) until the combined solution satisfies the original gyrokinetic Poisson equation. In more detail, introducing $\bar{\Phi} = \langle\Phi\rangle$ and $\tilde{\Phi} = \Phi - \bar{\Phi}$, we iterate the following system of equations:

$$\nabla_\perp \cdot \left(\frac{c^2 m_i n_i}{eB^2}\nabla_\perp \tilde{\Phi}^*_{n+1}\right) - Z_i\langle n_{i0}\rangle \frac{e\tilde{\Phi}^*_{n+1}}{T_e} = Z_i\langle n_{i0}\rangle - Z_i n_i - \nabla_\perp \cdot \left(\frac{c^2 m_i n_i}{eB^2}\nabla_\perp \bar{\Phi}_n\right), \tag{16}$$

$$\left\langle \nabla_\perp \cdot \left(\frac{c^2 m_i n_i}{eB^2}\nabla_\perp \bar{\Phi}_{n+1}\right)\right\rangle = Z_i\langle n_{i0}\rangle - Z_i\langle n_i\rangle - \left\langle \nabla_\perp \cdot \left(\frac{c^2 m_i n_i}{eB^2}\nabla_\perp \tilde{\Phi}_{n+1}\right)\right\rangle, \tag{17}$$

where $\tilde{\Phi}_{n+1} = \tilde{\Phi}^*_{n+1} - \langle\tilde{\Phi}^*_{n+1}\rangle$. During each iteration, the elliptic problem in Eq. (16) is solved by the generalized minimal residual (GMRES) method. Note that Eq. (16) for the non-zonal part of Φ does not involve nonlocal coupling, and therefore the GMRES Krylov method can be efficiently preconditioned by constructing a sparse diagonally dominated matrix corresponding to a lower-order (here, second-order) discretization of Eq. (16). The preconditioner problem is solved in COGENT by making use of parallel algebraic multi-grid (AMG) solvers implemented in the Hypre library.[34] For the applications considered in the present work, we adopt a second-order finite-volume discretization of the gyrokinetic Poisson model, and therefore the preconditioner is fully consistent with the GMRES problem. However, such low-order preconditioners are also found to be effective in high-order simulations, where a fourth-order discretization of the elliptic equations is used. The remaining zonal-flow equation [Eq. (17)] is a second-order one-dimensional ordinary differential equation that is straightforwardly solved by the direct inversion of the corresponding tri-diagonal matrices.

C. Vorticity model implementation

1. Stiff electron time scales

The vorticity model in Eq. (13) describes an electron response that is more detailed than the simple adiabatic relation [in Eq. (5)] used for the gyrokinetic Poisson equation. As a result, fast electron timescale processes with $\tau_{cond} \sim (k_\perp^2\rho_s^2)\tau_e(k_\parallel V_{Te}\tau_e)^{-2}$ appear in the vorticity model. Here, ρ_s is the ion gyroradius corresponding to the sound speed, $V_s \sim \sqrt{T_e/m_i}$, and $k_\perp$ and $k_\parallel$ are the wave-vectors for the perpendicular and parallel variations in the electrostatic potential, respectively. Considering moderately collisional electrons with $\tau_e \sim R_0/V_{Te}$, we obtain $\tau_{cond}^{\min} \sim (\rho_s/L_{d,\perp})^2(R_0/V_{Te})(R_0/h_\parallel)^{-2}$ for the fastest timescale supported by the simulation grid. Here, R_0 is the tokamak major radius, $h_\parallel$ is the cell size in the parallel direction, and $L_{d,\perp}$ is the perpendicular size of the simulation domain. These rapid processes associated with a strong parallel plasma conductivity are much faster than the ion time scales of interest such as the parallel transit time $\tau_{tr} \sim R_0/(qV_{Ti})$ and the drift-wave period $\tau_{dr} \sim (k_\perp\rho_i)^{-1}L_\perp/V_{Ti}$, and therefore have to be treated with implicit time integration techniques. Here, $L_\perp$ is the length scale for perpendicular variations in plasma profiles, and q is the magnetic safety factor. In the present work, the following simple first-order backward Euler scheme is used to advance the vorticity model in Eq. (13) subject to the isothermal electron response

$$\begin{aligned}\frac{\nabla_\perp \cdot \left(\frac{c^2 m_i n_i}{B^2}\nabla_\perp(\Phi^{l+1} - \Phi^l)\right)}{\Delta t} + \nabla \cdot \left(c\frac{-\nabla_\perp\Phi^l \times \mathbf{b}}{B}\varpi^l\right) &= \nabla \cdot \left(\frac{2\pi Z_i e}{m_i}\int \mathbf{v}_\perp^m f_i B_\parallel^* dv_\parallel d\mu\right) \\ &+ \nabla \cdot \left[\frac{cZ_i n_i T_e}{B}\left(\nabla \times \mathbf{b} + \frac{\mathbf{b}\times\nabla B}{B}\right)\right] \\ &+ B\nabla_\parallel\left[\frac{\sigma_\parallel}{B}\left(\frac{T_e}{en_i}\nabla_\parallel\left(n_i + \frac{\varpi^{l+1}}{Z_i e}\right) - \nabla_\parallel\Phi^{l+1}\right)\right].\end{aligned} \tag{18}$$

Here, Δt is a size of the time step, $t_l = \Delta t \cdot l$ corresponds to a discrete time variable, and the quantities in Eq. (18) that appear without a superscript are evaluated at the l^{th} time step. Note that a small time derivative of the ion density is neglected in Eq. (18). The vorticity model in Eq. (13) can also be advanced in time by making use of additive Runge–Kutta (ARK) methods that are available in the COGENT code.[35,36] The ARK approach provides consistent time integration for up to a fourth order in Δt, while treating the stiff terms implicitly. It also retains the ion density time derivative in the vorticity model. No pronounced difference is observed between the temporal discretization in Eq. (18) and the ARK method for the applications considered in this work. The former approach is, however, found to provide better computational performance and is, therefore, used for the production runs presented here.

Equation (18) is discretized with a second-order finite-volume method and is solved with the GMRES method. The GMRES solver is preconditioned by an elliptic problem derived from Eq. (18) by neglecting the polarization density corrections, $\varpi^{l+1}/(Z_i e)$, from the last line of Eq. (18). The preconditioner operator represents a strongly anisotropic elliptic problem, which is solved by making use of the AMG methods from the Hypre library.

2. Numerical pollution

The presence of the strongly anisotropic conductivity in Eq. (13) can lead to numerical pollution issues. Due to the large value of the parallel electron conductivity, the term, $\nabla \cdot (\mathbf{b}j_\parallel)$, dominates the RHS of Eq. (13) and enforces a nearly adiabatic electron response. However, on closed flux surfaces, where $\langle\nabla \cdot (\mathbf{b}j_\parallel)\rangle \equiv 0$, the radial electric field is set by the "perpendicular-physics" terms, e.g., $\langle\nabla \cdot \mathbf{j}_{\perp,i}\rangle$,

whose local values are small compared to $\nabla \cdot (\mathbf{b}j_{\parallel})$. If a numerical discretization scheme does not enforce a zero-flux surface average of the parallel current divergence, the corresponding truncation errors, e.g., due to grid misalignment with magnetic flux surfaces, can be comparable to (or larger) than $\langle \nabla \cdot \mathbf{j}_{\perp,i} \rangle$. The previous 4D COGENT studies[18] established a severe constraint on the level of grid misalignment in the X-point region required to maintain a tolerable truncation error in $\langle \nabla \cdot (\mathbf{b}j_{\parallel}) \rangle$. Those findings motivated the use of a globally flux-aligned grid for 4D simulations with self-consistent electric fields despite degraded convergence properties at the X-point. For the same reasons, our present 5D divertor version makes use of grid surfaces that are flux-aligned in the entire domain. However, while such grid construction was sufficient to maintain $\langle \nabla \cdot (\mathbf{b}j_{\parallel}) \rangle \equiv 0$ discretization on closed flux surfaces for the axisymmetric (4D) case, the lack of flux conservation at the block interfaces (see Sec. III A) can still result in sufficiently large truncation errors that can be comparable (or larger) than the physical terms (e.g., the Reynolds stress term or neoclassical guiding-center current), which govern the evolution of a radial electric field inside the separatrix. In more detail, the truncation error in the discrete evaluation of the parallel current flux-surface average can be estimated as

$$Err\{\langle \nabla \cdot (\mathbf{b}j_{\parallel}) \rangle\} \sim \frac{e\delta n V_{Te}}{qR_0} \frac{V_{Te}\tau_e}{qR_0} (k_\theta h_\theta)^n. \tag{19}$$

Here, k_θ is the poloidal wave-vector for density perturbation δn, h_θ is the poloidal cell size, and n is the order of the interpolation scheme used at block interfaces. We now compare this truncation error with the size of the Reynolds stress term, $\langle RS \rangle = \langle \nabla_\perp \cdot (c[\nabla_\perp \delta\Phi \times \mathbf{B}] \quad B^{-2}\delta\varpi]) \rangle \sim c^3 n_i m_i B^{-3} k_\perp^4 \delta\Phi^2$. Adopting the standard ordering, $k_\perp \rho_i \sim k_\theta \rho_i \sim 1$ and $\delta n/n \sim e\delta\Phi/T_e \sim \rho_i/L_p$, where L_p is the length scale for variations in background quasi-equilibrium, the condition required for accurate modeling, i.e., $Err\{\langle \nabla \cdot (\mathbf{b}j_{\parallel}) \rangle\} \ll \langle RS \rangle$, corresponds to

$$\left(\frac{h_\theta}{\rho_i}\right)^n \ll \frac{qR_0}{\tau_e V_{Te}} \frac{qR_0}{L_p} \left(\frac{T_e}{T_i}\right)^2 \frac{V_{Ti}}{V_{Te}}. \tag{20}$$

Considering parameters characteristic of DIII-D edge plasmas, $n_e \sim 10^{19}\mathrm{m}^{-3}$, $q \sim 3$, $R_0 \sim 1.6\mathrm{m}$, $T_i \sim 300\mathrm{eV}$, $T_e \sim 50\mathrm{eV}$, $B \sim 1.6\mathrm{T}$, $B_\theta/B \sim 0.2$, we obtain a strenuous constraint on the poloidal size of computational cells, $(h_\theta/\rho_i)^n \ll 10^{-3} \times qR_0/L_p$, which is more severe than the basic constraint on adequate representation of the turbulence perturbations, $h_\theta/\rho_i \ll 1$. To avoid the use of such overly constrained cell size, the present implementation of the RHS of Eq. (18) includes the pollution correction term, $-\langle \nabla \cdot (\mathbf{b}j_{\parallel}) \rangle_{num}$, which corresponds to a numerical evaluation of the flux-surface averaged parallel current. This correction is only introduced inside the magnetic separatrix, and as a result, the flux surface average of Eq. (18) does not contain any contributions from the parallel current on closed field lines.

In Sec. IV C, we illustrate the numerical pollution issues with a practical ITG simulation. While no pronounced effects of the numerical pollution are observed during the linear stage, which is primarily governed by the adiabatic electron response, spurious numerical results are observed during the nonlinear stage of the ITG instability if the condition $\langle \nabla \cdot (\mathbf{b}j_{\parallel}) \rangle \equiv 0$ is not discretely enforced on closed flux surfaces. Finally, it is worthwhile to mention that the numerical pollution in the vorticity model discussed here can also be of importance to drift-reduced fluid numerical simulations that either do not use field-aligned coordinates[37] or use interpolation to obtain boundary condition for the field-aligned coordinate.[32]

D. Temporal discretization

In the present work, a fourth-order Runge-Kutta method is used to advance the gyrokinetic equation [Eq. (1)] in time. We also note that an implicit-explicit (ImEx) time integration algorithm is available in COGENT.[35,36] It is based on semi-implicit additive Runge-Kutta (ARK) methods and can provide consistent high-order time integration, including implicit treatment of selected stiff terms. The ImEx algorithm employs the Newton-Krylov approach to handle nonlinearities, and it utilizes preconditioning to improve convergence properties. A successful application of the ImEx approach to simulations of strongly collisional plasmas with nonlinear Fokker-Planck collision model is reported in Ref. 36. In that work, the collisional term is integrated implicitly in time, while the advective term is treated explicitly, thus allowing time step sizes that are comparable to the advective time scales. Our current efforts are focused on developing implicit capabilities to handle stiff kinetic electron response. As a first step, the ARK method is applied to implicit time integration of the 5D gyrokinetic Vlasov advection operator for the case of a fixed electrostatic potential and a single-null geometry. The convergence properties of the Krylov (here, GMRES) solver are improved by utilizing a preconditioner corresponding to a lower-order (e.g., first-order upwind) discretization of the advection operator, which is, in turn, inverted by making use of the pAIR AMG methods from the Hypre library.[34] While additional developments are needed to efficiently handle the stiff electrostatic Alfvén timescale[38] once kinetic electrons are included, the present implicit capabilities are demonstrated to provide a substantial speed-up the gyrokinetic simulations with a reduced electron model by relaxing the Courant constraint for the gyrokinetic Vlasov advection. The corresponding results will be reported in our future publications.

IV. VERIFICATION STUDIES

This section presents the results of verification studies in toroidal annulus and slab geometries. Section IV A reports on ITG simulations performed with the gyrokinetic Poisson model in Eq. (4). Verification of the vorticity model in Eq. (18) is presented in Secs. IV B and IV C by considering test problems involving the ITG and resistive drift instabilities, respectively. Finally, Sec. IV D demonstrates the numerical pollution issue [see Sec. III C 2] with a practical ITG simulation.

With the exception of Sec. IV C, the simulations are performed in a circular concentric tokamak configuration specified by

$$\mathbf{B} = \frac{I}{R}\left(\frac{r}{q(r)R_0}\mathbf{e}_\theta + \mathbf{e}_\phi\right), \tag{21}$$

where $(r, \phi, \text{and } \theta)$ represent the toroidal coordinate system, R is the major radius coordinate, R_0 is the radial distance between the tokamak axis and the core center, and $I = RB_\phi = const$. Following the analysis in Refs. 4 and 39, we define the magnetic safety factor profile as

$$q(r) = q_0 + q_1 \exp\left(q_2 \log \frac{r}{a}\right), \tag{22}$$

where a denotes the minor radius constant. The locally aligned coordinate system is introduced within each block as follows: the radial coordinate $\xi_0 = r$ labels a flux surface, the field-aligned coordinate $\xi_1 = \phi$ designates the position along a field-line as measured by the toroidal angle, and finally, the "poloidal" coordinate ξ_2 that labels a field line is defined by

$$\xi_2 = 2\arctan\left(\frac{1+\bar{r}}{\sqrt{1-\bar{r}^2}}\tan\left(\Theta - \frac{\sqrt{1-\bar{r}^2}}{2}\frac{\phi-\phi_n}{q(\bar{r})}\right)\right). \quad (23)$$

Here $\bar{r} = r/R_0$, $\Theta = \arctan\left(\frac{\sqrt{1-\bar{r}^2}}{1+\bar{r}}\tan\frac{\theta}{2}\right)$, and ϕ_n designates the reference poloidal plane in block n (here taken as the toroidal center of a block), where $\xi_2 = \theta$.

The constant parameters in Eqs. (21)–(23) are specified as $R_0 = 1.68\text{m}$, $a = 0.6\text{m}$, $I = RB_\phi = 3.5\text{Tm}$, $q_0 = 1.0$, $q_1 = 2.78$, and $q_2 = 2.8$, and the radial simulation domain spans $0.19\text{m} \le r \le 0.41\text{m}$, such that at the middle of the radial domain, $r_{mid} = a/2$, $\bar{q} \equiv q(r_{mid}) = 1.4$ and $s(r_{mid}) = (r_{mid}/\bar{q})q'(r_{mid}) = 0.8$. Finally, a singly charged, $Z_i = 1$, deuterium, $m_i = 2m_p$, ion species, with m_p denoting the proton mass, is considered in all simulations presented in this paper.

A. ITG simulations with the gyrokinetic Poisson model

The simulation model in Eq. (1) and Eqs. (4)–(5) is used here for simulations of the ITG turbulence and the associated plasma transport. The COGENT implementation of the gyrokinetic Poisson model has been previously verified[19] against the well-known linear Cyclone base case (CBC) test,[40] and the present studies are focused on the analysis of nonlinear plasma transport involving profile relaxation. While the gyrokinetic Vlasov–Poisson model is customarily used in full-F core codes,[30] its physical limitations have recently been pointed out in Refs. 26–28. In this work, this model is primarily used as a testbed for COGENT numerical algorithms and their efficiency.

Following the verification studies in Ref. 41, we take the initial plasma distribution as a local Maxwellian distribution with density and temperature profiles specified by the following functional form:

$$A(\psi) = A_0\left(\frac{\cosh\left[(\psi-\psi_{mid}+\delta_A)/\Delta_A\right]}{\cosh\left[(\psi-\psi_{mid}-\delta_A)/\Delta_A\right]}\right)^{-\kappa_A\Delta_A/2}, \quad (24)$$

here, $\psi = \psi(r)$ is the magnetic flux function that satisfies $\psi' \equiv d\psi/dr = RB_\theta$ subject to a $\psi(0) = 0$ boundary condition, $\psi_{mid} \equiv \psi(r_{mid})$, and

$$\kappa_A = \left[\psi'(r_{mid})L_A\tanh\left(\frac{\delta_A}{\Delta_A}\right)\right]^{-1}, \quad (25)$$

where $L_A = A/A'(r_{mid})$ is the inverse logarithmic derivative measured at the middle of the radial domain, and $A' \equiv dA/dr$. The constant parameters in Eqs. (24) and (25) are given for the initial plasma ion density ($A = N$) and temperature ($A = T$) profiles by $T_0 = 1.75\text{keV}$, $N_0 = 10^{14}\text{cm}^{-3}$, $R_0/L_N = 2.2$, $R_0/L_T = 12$, $\delta_N = \delta_T = 2.7 \times 10^{-2}\text{Tm}^2$, and $\Delta_N = \Delta_T = 4.54 \times 10^{-3}\text{Tm}^2$. The electron temperature in Eq. (5) is taken to be uniform, $T_e = T_0$. Note that a local Maxwellian distribution does not correspond to an equilibrium for the full-F gyrokinetic model, and therefore, initial long-wavelength transients are expected. We further perturb the initial distribution by introducing density perturbations with an amplitude of 0.3% and toroidal and poloidal harmonic numbers of $n = 20$ and $m = 28$, respectively. Such perturbation corresponds to $k_\theta\rho_i = n\bar{q}\rho_i/r_{mid} = 0.27$ and a nearly maximal growth rate in the ITG spectrum.[40]

A simple linearized collision model describing ion-ion collisions with a fixed Maxwellian background is included in the simulations

$$C\left[B_\parallel^*\delta f_i\right] = \frac{1}{2}\nu_D(x)\frac{\partial}{\partial\xi}\left(1-\xi^2\right)\frac{\partial B_\parallel^*\delta f_i}{\partial\xi} + \frac{1}{2}\frac{1}{\mathrm{v}^2}\frac{\partial}{\partial\mathrm{v}}\left\{\mathrm{v}^3\left[\nu_s(x)B_\parallel^*\delta f_i + \nu_\parallel(x)\mathrm{v}\frac{\partial B_\parallel^*\delta f_i}{\partial\mathrm{v}}\right]\right\}. \quad (26)$$

Here, δf_i is a deviation of the ion distribution function from the initial Maxwellian distribution, $\xi = \mathrm{v}_\parallel/\mathrm{v}$, $\mathrm{v} = \left(\mathrm{v}_\parallel^2 + 2\mu B/m_i\right)^{1/2}$, $x = \mathrm{v}/\sqrt{2T_0/m_i}$, and the standard definitions for the relaxation rates, ν_D, ν_s, and $\nu_\parallel$ are used.[42] Implementation of this collision model in COGENT along with more comprehensive collision options is described in detail in Ref. 14. The simplified collision model in Eq. (26) does not conserve parallel momentum or energy, which limits its validity. However, for the plasma parameters considered here, the effect of collisions measured by $\bar{q}R_0/(\tau_i V_{Ti}) \approx 0.007$ is weak, and no pronounced difference in the simulation results was observed for the corresponding collisionless case. Indeed, the collisional neoclassical heat flux estimated in a weakly collisional regime as[42]

$$q_{NC} \approx 1.35\sqrt{\frac{r_{mid}}{R_0}}\frac{N_0T_0^2}{m_i\Omega_{i\theta}^2\tau_i L_T}, \quad (27)$$

is about 20 times smaller than the turbulence-driven heat flux discussed below. Here, τ_i is the basic ion collisional time given by Braginskii[24] and $\Omega_{i\theta} = Z_ieB_\theta/m_ic$.

The results of the numerical simulations are shown in Figs. 3–5. Figures 3 and 4 illustrate simulations in a toroidal wedge of $\Delta\phi = \pi/2$, where periodicity is imposed at the toroidal boundaries and a single computational block is used in the toroidal direction. Numerical convergence in the radial, r, and poloidal, θ, directions is studied by performing simulations with $(N_r, N_\theta) = (48, 256)$, $(N_r, N_\theta) = (96, 512)$, and $(N_r, N_\theta) = (192, 1024)$. Here, N_α denotes the number of grid points in the phase-space direction α. The grid resolution in the other directions is given by $N_\phi = 4$, $N_{\mathrm{v}_\parallel} = 48$, and $N_\mu = 32$. The velocity domain extent corresponds to $-4.9V_{T0} \le \mathrm{v}_\parallel \le 4.9V_{T0}$ and $0 \le \mu \le 10.4T_0R_0/I$, where $V_{T0} = \sqrt{T_0/m_i}$. The consistent boundary condition in Eq. (15) is used for electrostatic potential variations at the radial boundaries. This alleviates the need for radial buffer regions, which have been previously used in analogous full-F continuum gyrokinetic modeling (see, for instance, Refs. 4, 29, and 30).

The radial lineouts at the outer midplane for the instantaneous values of the potential and ion temperature show good convergence properties [see Figs. 4(a) and 4(b)]. The mapped-space volume average, $\bar{Q} \equiv \langle Q_r\rangle_{vol}$, of the characteristic wedge-weighted radial transport power

$$Q_r = \left\langle\int\frac{2\pi}{m_i}B_\parallel^*d\mathrm{v}_\parallel d\mu\left(m_i\mathrm{v}_\parallel^2/2 + \mu B/m_i + Z_ie\Phi\right)\left(\dot{\mathbf{R}}\cdot\mathbf{e}_\mathbf{r}\right)f_i\right\rangle\frac{\Delta\phi}{2\pi}\mathrm{S}_\parallel, \quad (28)$$

shows excellent convergence during initial transient perturbations, while a moderate difference appears later on as the short-scale turbulence develops [see Fig. 4(c)]. Here, the mapped-space volume average

$$\langle\chi\rangle_{vol} \equiv \frac{1}{N_rN_\phi N_\theta}\sum_{i,j,k}\chi_{i,j,k} \quad (29)$$

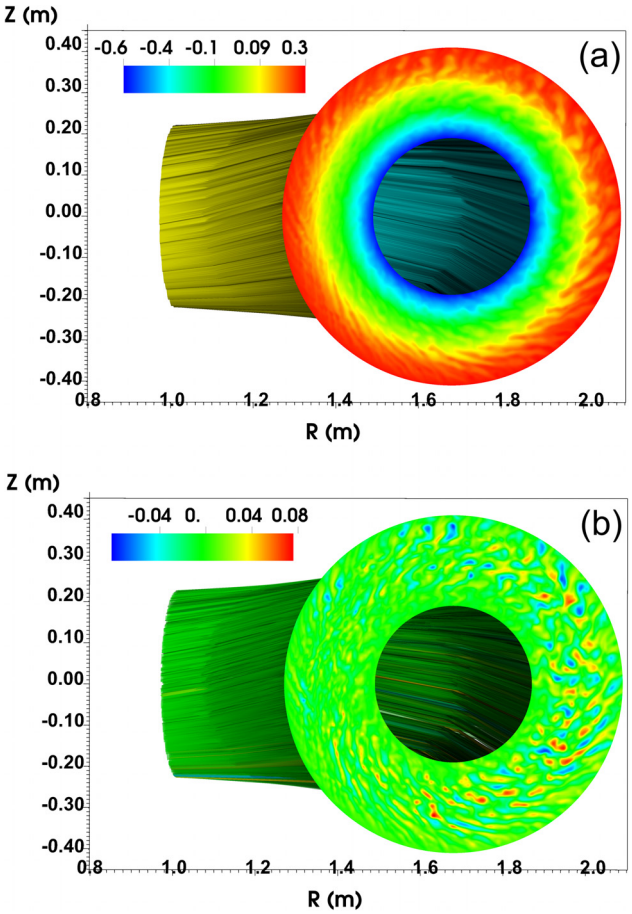

FIG. 3. Full-F simulations of the ITG turbulence with the local Maxwellian initialization. Shown are the electrostatic potential variations, $e\Phi/T_e$ [frame (a)], and its non-zonal component, $e(\Phi - \langle\Phi\rangle)/T_e$ [frame (b)] at the time instance corresponding to $t = 35.7R_0/V_{T0}$. A periodic toroidal wedge of $\Delta\phi = \pi/2$ is considered, and the gyrokinetic Poisson model in Eqs. (4) and (5) is used for self-consistent potential variations.

corresponds to a sum over the spatial indices divided by the total number of spatial cells and $S_{\text{mid}} = 4.0\ \pi^2\ r_{\text{mid}}R_0$ is the characteristic magnetic flux surface area. More detailed analysis of the numerical convergence properties during the turbulence regime should involve additional statistical averaging (e.g., time integration) and will be a subject of future work.

Figure 5 illustrates the results of full-torus simulations, $\Delta\phi = 2\pi$. Numerical convergence in the toroidal (i.e., field-aligned) coordinate, ϕ, is studied by dividing the toroidal domain into two, four, and eight toroidal blocks, while maintaining 4 toroidal cells per block. Rapid convergence can be observed in Fig. 5(d), illustrating the mapped-space volume-averaged value of the effective energy of the non-zonal potential component. Moreover, the mode structure is well-captured even at the most coarse resolution level [compare Figs. 5(a)–5(c)]. Note that the intermediate grid resolution of 16 toroidal cells for the full-torus simulations corresponds to the toroidal resolution of four cells used in the wedge simulations with $\Delta\phi = \pi/2$ shown in Fig. 4. The results of the simulations in Fig. 5 demonstrate the efficiency of the locally field-aligned coordinate system. Indeed, the strongly anisotropic ITG turbulence [see Figs. 3–5] is characterized by $k_\parallel \sim 1/qR_0$ and $k_\perp \sim 1/\rho_i$, or, equivalently, by the toroidal mode number of $n_{tb} \sim r_{mid}/(\bar{q}\rho_i)$. For the parameters of the simulations presented here, we obtain $n_{tb} \approx 74$, and therefore, the standard toroidal coordinates grid system would require 74 times more toroidal points (assuming the use of 16 grid points per a single harmonic) for the equivalent simulation.

B. ITG simulations with the vorticity model

The vorticity model in Eq. (18) is verified here by performing ITG simulations and comparing the results against the analogous simulations using the gyrokinetic Poisson model. To minimize the effects of initial axisymmetric transients and large-amplitude radial electric fields [see Fig. 4(a)], we neglect collisions and initialize the simulations with an equilibrium solution to the full-F gyrokinetic equation for the case of a zero electrostatic potential. The guiding-center equilibrium distribution corresponding to a zero electric field should depend only on the invariants of motion: energy $(E = m_i v_\parallel^2/2 + \mu B)$, magnetic moment (μ), and the canonical angular momentum $(P_\phi = Z_i e\psi/c + m_i v_\parallel RB_\phi/B)$. It is evident that a locally Maxwellian distribution

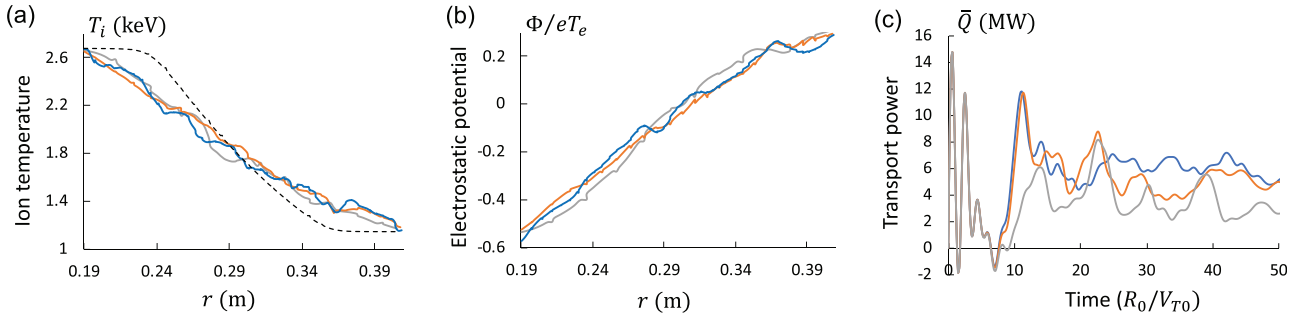

FIG. 4. Full-F simulations of the ITG turbulence with the local Maxwellian initialization. Numerical convergence in the radial and poloidal directions is studied for (a) ion temperature radial profile, (b) electrostatic potential radial profile, and (c) the wedge-weighted transport power by performing simulations with $(N_r, N_\theta) = (48, 256)$ (gray curve), $(N_r, N_\theta) = (96, 512)$ (orange curve), and $(N_r, N_\theta) = (192, 1024)$ (blue curve). The time instance for the results in frames (a) and (b) corresponds to $t = 35.7R_0/V_{T0}$. The initial ion temperature profile is shown in frame (a) with the dashed black cure. Periodic toroidal wedge of $\Delta\phi = \pi/2$ is considered, and the gyrokinetic Poisson model in Eqs. (4)–(5) is used for self-consistent potential variations.

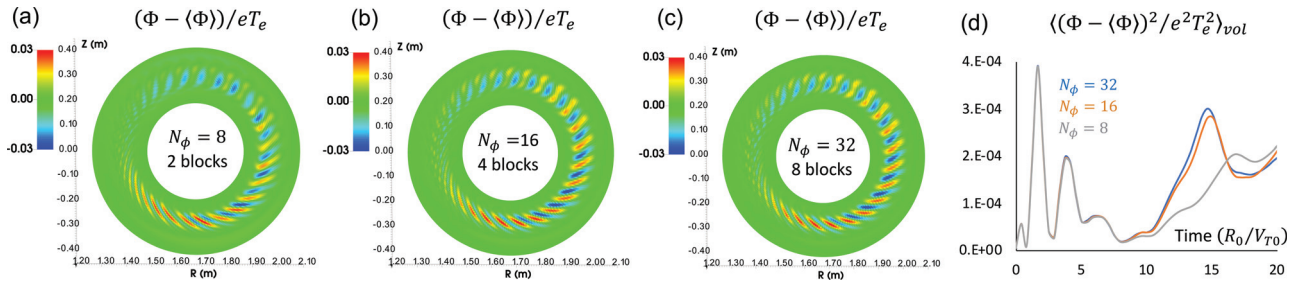

FIG. 5. Full-F simulations of the ITG turbulence with the local Maxwellian initialization. Numerical convergence in the toroidal (i.e., field-aligned) coordinate is studied for the non-zonal component of an electrostatic potential by performing simulations with (a) $N_\phi = 8$, (b) $N_\phi = 16$, and (c) $N_\phi = 32$ toroidal cells, while maintaining 4 toroidal cells per block. The plots in Frames (a)-(c) correspond to the time instance of $t = 10.5R_0/V_{T0}$. Frame (d) shows the time history for the mapped-space volume-average of the effective non-zonal component energy for $N_\phi = 8$ (gray curve), $N_\phi = 16$ (orange curve), and $N_\phi = 32$ (blue curve). Full-torus simulations, $\Delta\phi = 2\pi$, are considered, and the gyrokinetic Poisson model in Eqs. (4) and (5) is used for self-consistent potential variations.

function $F_{LM} = [2\pi T(\psi)/m_i]^{-3/2} N(\psi)\exp[-m_i v_\parallel^2/2T(\psi) - \mu B/T(\psi)]$ can be turned into an equivalent canonical Maxwellian F_{CM} equilibrium function by replacing ψ with

$$\psi_{inv} = \psi + \frac{m_i c}{Z_i e}\frac{RB_\phi}{B} v_\parallel, \tag{30}$$

such that in the limit $\rho_i/L_{N,T} \ll 1$, we recover $N(\psi) \approx N(\psi_{inv})$ and $T(\psi) \approx T(\psi_{inv})$. This approach is used here to initialize the ion distribution. The initial plasma profiles are specified by

$$A(\psi_{inv}) = A_0 \exp\left[-\kappa_A \Delta_A \tanh\left(\frac{\psi_{inv} - \psi_{mid}}{\Delta_A}\right)\right], \tag{31}$$

where $\kappa_A = 1/[L_A \psi'(r_{mid})]$. The functional form in Eq. (31), which is also used in Ref. 39, is adopted here instead of that used in Eq. (24), as it is observed to generate less perturbation in plasma profiles when ψ is replaced with ψ_{inv}. The initial density and temperature profiles are set by using $N_0 = 10^{14}\text{cm}^{-3}$, $T_0 = 7k\text{eV}$, $R_0/L_N = 5.14$, $R_0/L_T = 16$, and $\Delta_N = \Delta_T = 1.8 \times 10^{-2}\text{Tm}^2$, and the initial value of the electrostatic potential is set to zero.

For this test simulation, we consider a periodic wedge of $\Delta\phi = 0.2\pi$ and use a single toroidal block. The fundamental mode $n = 2\pi/\Delta\phi = 10$ and the associated $k_\theta \rho_i = n\bar{q}\rho_i/r_{mid} = 0.27$ correspond to a nearly maximal growth rate in the ITG spectrum. For simplicity, a zero Dirichlet boundary condition is used for the electrostatic potential at both radial boundaries. As in Sec. IV A, we perturb the initial distribution by introducing density perturbations with an amplitude of 0.3% and toroidal and poloidal harmonic numbers of $n = 10$ and $m = 14$, respectively. The grid resolution is taken to be $[N_\psi = 96, N_\phi = 4, N_\theta = 512, N_{v_\parallel} = 48, N_\mu = 32]$, and the velocity domain extent is $-4.9V_{T0} \le v_\parallel \le 4.9V_{T0}$ and $0 \le \mu \le 10.4T_0R_0/I$, where $V_{T0} = \sqrt{T_0/m_i}$.

For both, the gyrokinetic Poisson model in Eqs. (4) and (5) and the vorticity model in Eq. (18), a uniform electron temperature, $T_e = T_0$, is considered. Furthermore, the vorticity model adopts a uniform parallel conductivity given by

$$\sigma_\parallel = 1.96 N_0 e^2 \frac{\bar{\tau}_e}{m_e}, \tag{32}$$

where the $\bar{\tau}_e$ parameter is chosen such that $\bar{\tau}_e \omega_{tr,e} = 10$. Here, $\omega_{tr,e} = \sqrt{T_e/m_e}/(\bar{q}R_0)$ is the electron transit frequency. Note that Braginskii's formulation of the parallel conductivity in Eq. (11) is only valid in the collisional regime, $\bar{\tau}_e \omega_{tr,e} \ll 1$, and an increase in the collision time $\bar{\tau}_e$ is limited by the inverse electron transit frequency $\omega_{tr,e}^{-1}$ in a hot collisionless plasma. Here, we choose an artificially high value of $\bar{\tau}_e$ to improve consistency between the vorticity model and the adiabatic electron response in Eq. (5).

The results of these numerical simulations demonstrate good agreement between the gyrokinetic Poisson and vorticity models (see Fig. 6). For better consistency with the first-order backward Euler time integration of the vorticity model [see Eq. (18)], the electric potential in Eq. (4) is only updated once per a time step. This, however, results in minimal differences as compared to the consistent fourth-order time integration of the gyrokinetic Poisson model. Figures 6(a) and 6(b) show variations of the electrostatic potential in the poloidal plane. In contrast to the ITG simulations performed in Sec. IV A for the case of a local Maxwellian initialization [see Figs. 3(a) and 3(b)], the use of canonical Maxwellian initialization mitigates the development of strong axisymmetric radial electric fields. Note that a pronounced initial value of the $\langle(e\Phi/T_e)^2\rangle_{vol}$ quantity illustrated in Fig. 6(c) is due to the fact that the initial canonical Maxwellian distribution with the plasma profiles in Eq. (31) yields axisymmetric poloidal variations of the order $O(\rho_i/L_{N,T})$ in a local ion density. Such density perturbations generate the corresponding potential variations [as can be readily seen from Eqs. (4) and (5)], and therefore, the initial distribution function that corresponds to a full-F equilibrium solution to Eq. (1) in the absence of electric fields can only serve as an approximate equilibrium once the self-consistent potential variations are included.

C. Resistive drift mode simulations with the vorticity model

In Sec. IV B, the vorticity model is shown to agree well with the gyrokinetic Poisson model in the simulations of the ITG instability for the case of hot core plasmas characterized by an adiabatic electron response [see Eq. (5)]. However, in contrast to the gyrokinetic Poisson model with adiabatic electrons, the vorticity model also supports resistive drift modes that play an important role in a cold tokamak edge. For the purpose of COGENT verification, the following simplified test problem is considered here.

A uniform magnetic field is considered, $\mathbf{B} = B\mathbf{e}_z$, and a Cartesian coordinate system with the basis triad $(\mathbf{e}_x, \mathbf{e}_y, \mathbf{e}_z)$ is used.

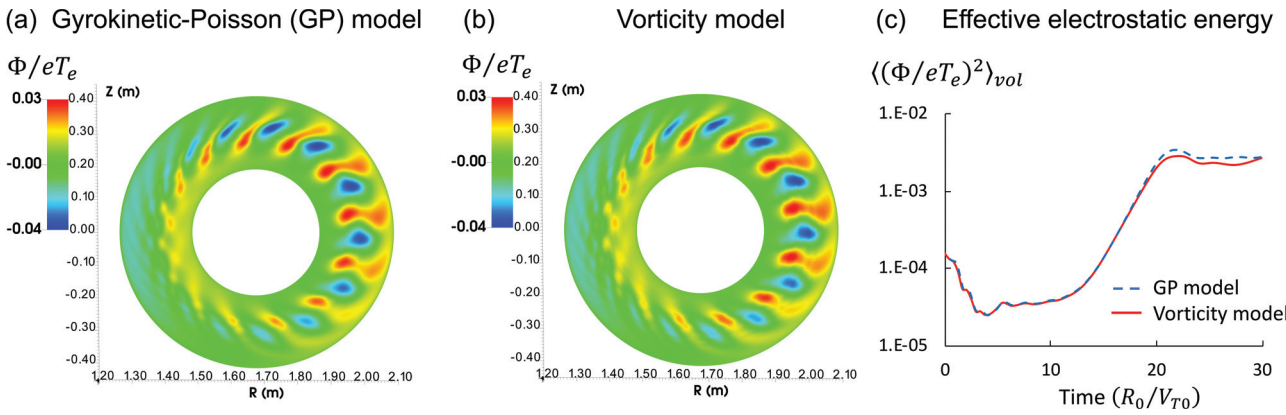

FIG. 6. Full-F simulations of the ITG instability with the canonical Maxwellian initialization. Shown is a comparison between the gyrokinetic-Poisson and vorticity models for the potential variations in the poloidal plane at $t = 14.7R_0/V_{T0}$ [frames (a) and (b)], and the time history of the mapped-space volume-averaged effective electrostatic energy [frame (c)]. An artificially enhanced value of the uniform plasma conductivity corresponding to $\bar{\tau}_e\omega_{tr,e} = 10$ is considered.

Following analogous verification studies reported elsewhere,[43] we neglect the parallel acceleration and the ion collision effects in Eq. (1), as well as the effects of the perpendicular currents in Eq. (13). The corresponding simulation model is given by

$$\frac{\partial f_i}{\partial t} + \nabla\cdot\left(c\frac{-\nabla\Phi\times\mathbf{B}}{B^2}f_i\right) = 0, \tag{33}$$

$$\frac{\partial \varpi}{\partial t} = \nabla_\parallel\left[\sigma_\parallel\left(\frac{T_e}{eZ_in_i}\nabla_\parallel n_e - \nabla_\parallel\Phi\right)\right], \tag{34}$$

where we retain the difference between the electron and guiding-center ion densities, i.e., $n_e = Z_in_i + e^{-1}\varpi$ in the vorticity equation. Adopting $Z_i = 1$ and allowing variations in the plasma density with the characteristic length scale, $L_N = n_i(dn_i/dx)^{-1} < 0$, the model in Eqs. (33) and (34) yields the following local dispersion relation for short-scale perturbations, proportional to $\exp(i\omega t + ik_yy + ik_zz)$, with $|k_yL_N| \gg 1$

$$\left(\frac{\omega}{\omega^*}\right)^2 - i\frac{\sigma_\parallel^*}{\omega^*}\left(\frac{\omega}{\omega^*} - 1\right) = 0. \tag{35}$$

Here, $\sigma_\parallel^* = 1.96\tau_e(k_z/k_y)^2\Omega_i\Omega_e(1+k_y^2\rho_s^2)$, $\omega^* = (1+k_y^2\rho_s^2)^{-1}ck_yT_e/(eBL_N)$, $\rho_s = \sqrt{T_e/m_e}\Omega_e^{-1}$, and $\Omega_e = eB/m_ec$, and we assumed that $k_y \gg k_x$.

The analytical solution to the dispersion relation in Eq. (35) is recovered in the COGENT simulations (see Fig. 7) that adopt a local Maxwellian distribution with a uniform temperature, $T_i = T_e$, and a density profile given by $n_i = N_0\exp(-x/|L_N|)$, where $\rho_s/|L_N| = 3.8\times10^{-3}$, $k_y\rho_s = 1.2$, and $k_z\rho_s = 1.4\times10^{-4}$. The simulations consider conducting (grounded) boundaries in the x-direction and periodic boundary conditions in the y and z directions. The spatial domain extent is given by $L_x = 66\rho_s$, $L_y = 2\pi/k_y$, and $L_z = 2\pi/k_z$, and all harmonics other than the fundamental one are filtered out from the electrostatic potential distribution in the periodic directions y and z after each solve of Eq. (34). The velocity domain extent is given by $-3.5\sqrt{2T_i/m_i} \le v_\parallel \le 3.5\sqrt{2T_i/m_i}$ and $0 \le \mu \le 5T_i/B$. The grid resolution is given by $(N_x, N_y, N_z, N_{v_\parallel}, N_\mu) = (36, 16, 16, 32, 24)$, and the time step corresponds to $\Delta t\omega^* = 0.043$. Figure 7 shows the results of the COGENT simulations for different values of a uniform normalized parallel conductivity parameter spanning the range of $0.1 < \sigma_\parallel^*/\omega^* < 10$.

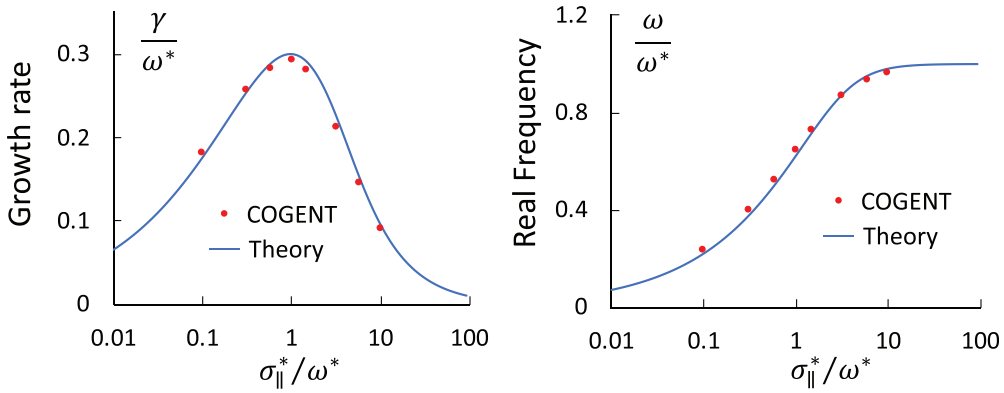

FIG. 7. Resistive drift mode simulations with the vorticity model. The results of the COGENT simulations (red dots) are compared with an analytical solution to the dispersion relation in Eq. (35) (blue curves).

D. Numerical pollution in the vorticity model

Here, we provide a practical illustration of the numerical pollution issue (see Sec. III A) related to the mismatch in the field-aligned grids at the toroidal block interfaces and the presence of a strongly anisotropic conductivity in the vorticity model [see Eq. (13)]. Clearly, the numerical pollution can be arbitrary exaggerated by increasing the value of the parallel conductivity, and the purpose of this analysis is to demonstrate the issue for practical simulation parameters. For that reason, we consider the same simulation parameters as those used in Sec. IV B; however, the value of the effective electron collision time is decreased tenfold to $\bar{\tau}_e\omega_{tr,e} = 1$, such that the corresponding value of the parallel conductivity in Eq. (32) can be used as a "flux-limited" approximation for a hot (weakly collisional) core plasma regime. In addition, the simulations presented in this section employ the self-consistent boundary condition [see Eq. (15)] at the inner radial boundary and make use of the fourth-order centered-difference discretization of the Vlasov equation with WENO-like limiter modifications[44] as a demonstration of a higher-order capability.

To illustrate the numerical pollution issue, the results of COGENT simulations including (as described in Sec. III A) or omitting the pollution error corrections are presented in Fig. 8. Recall that the pollution is related to truncation errors from 1D poloidal remapping of field-aligned grids. Therefore, two cases of the poloidal grid resolution, i.e., "high" $N_\theta = 512$ and "low" $N_\theta = 256$, are considered here. Other grid resolution parameters are given by $(N_r, N_\phi, N_{v_\parallel}, N_\mu) = (48, 8, 32, 24)$. No pronounced difference is observed during the linear stage [see Fig. 8(a)], whether the numerical correction is included or not. This result can be explained by the fact that the linear stage of the ITG instability is primarily determined by the "parallel" quasi-adiabatic response, which is set by the dominant term in Eq. (18), i.e., $\nabla \cdot (\mathbf{b} j_\parallel) \approx 0$. However, substantially degraded numerical convergence in the absence of the pollution error corrections is evident already during an early nonlinear stage, where the subdominant "radial" terms play an important role [see Fig. 8(b)]. More detailed analysis of the convergence properties is presented in Fig. 9, illustrating the outer midplane radial line-out of the potential during the nonlinear stage. The small quantitative difference between the high- and low-resolution cases observed in the presence of the pollution error corrections can be attributed to exponential separation of close phase-space trajectories for the case of a physically unstable system. Indeed, changing the diagnostic time instance used for the low-resolution case by only 5% brings the results much closer to the high-resolution case. In contrast, if the pollution error corrections are not included, the low-resolution case yields a qualitatively spurious result.

V. ION TURBULENCE SIMULATIONS IN A SINGLE-NULL GEOMETRY

The full-F gyrokinetic equation [Eq. (1)] coupled to the hybrid gyrokinetic ion-fluid electron vorticity model for electrostatic potential variations [Eq. (18)] is used here to perform ion-scale turbulence simulations in a single-null geometry. For simplification purposes, ion–ion collisions are neglected, and a model single-null magnetic geometry is considered. The axisymmetric single-null geometry used in this work corresponds to the following model flux function:

$$\Psi(R,Z) = \Psi_{CORE}(R,Z) - \Psi_{CORE}(R_0,0) + \bar{\Psi}(R,Z) - \bar{\Psi}(R_0,0). \tag{36}$$

Here, R and Z are the cylindrical coordinates, $\Psi_{CORE}(R,Z)$ is the flux function corresponding to a toroidal annulus geometry with concentric flux surfaces

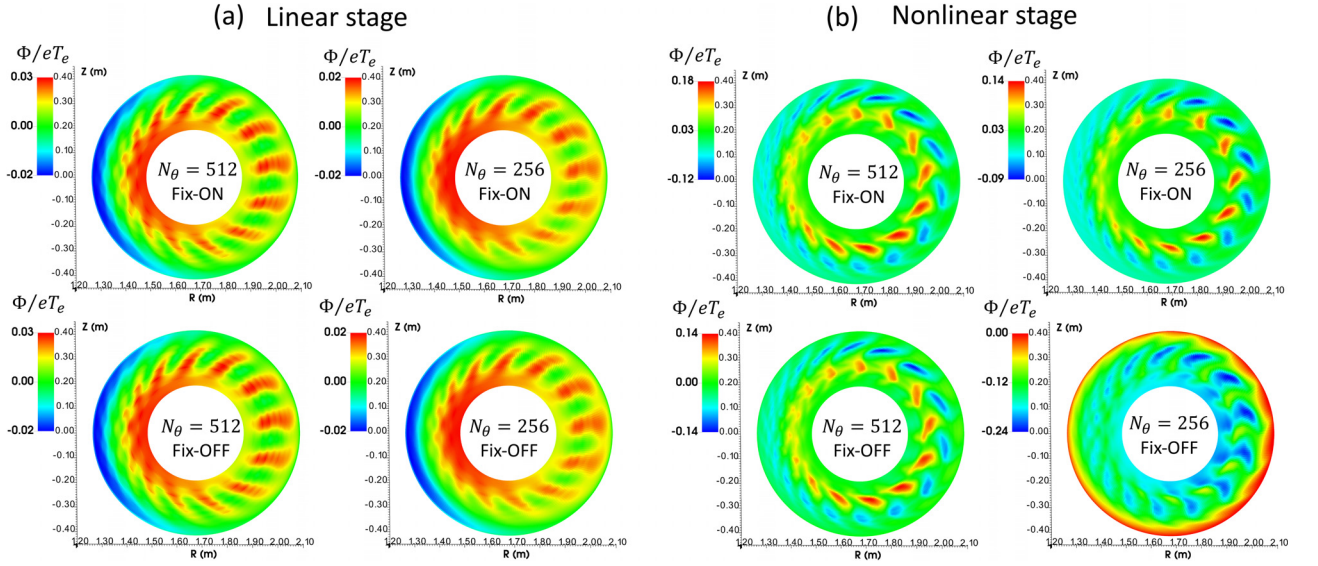

FIG. 8. Illustration of the numerical pollution issue for the full-F simulations of the ITG instability with the canonical Maxwellian initialization and a uniform parallel conductivity corresponding to $\bar{\tau}_e\omega_{tr,e} = 1$. The simulations with the pollution-error corrections included (designated by the "fix-ON" label) and not included (designated by the "fix-OFF" label) are performed for the cases of $N_\theta = 256$ and $N_\theta = 512$. Shown are the potential variations, $e\Phi/T_e$, at the linear stage corresponding to $t = 11.34R_0/V_{T0}$ [frame (a)], and at the early nonlinear stage corresponding to $t = 18.9R_0/V_{T0}$ [frame (b)]. Notice the spurious numerical solution obtained in the simulations where the pollution error corrections are not included and $N_\theta = 256$ [lower right panel in frame (b)].

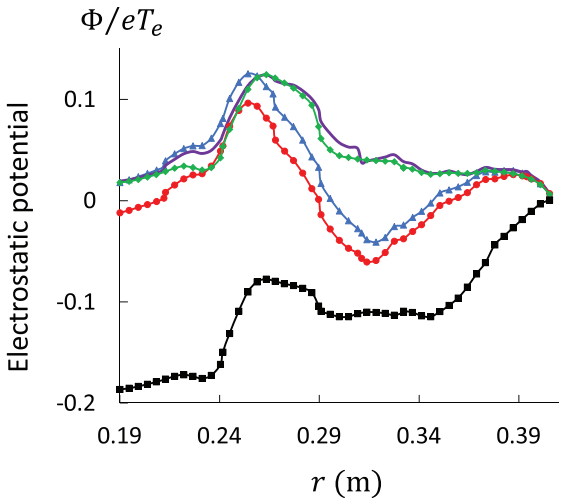

FIG. 9. Radial lineout of the electrostatic potential variations at the early nonlinear stage ($t = 18.9R_0/V_{T0}$) corresponding to $N_\theta = 512$ with "fix-ON" (blue triangles), $N_\theta = 256$ with "fix-ON" (green diamonds), $N_\theta = 512$ with "fix-OFF" (red circles), and $N_\theta = 256$ with "fix-OFF" (black squares). In addition, the radial potential profile for the case of $N_\theta = 512$ with "fix-ON" is shown at the slightly earlier time instance corresponding to $t = 17.95R_0/V_{T0}$ (solid purple curve).

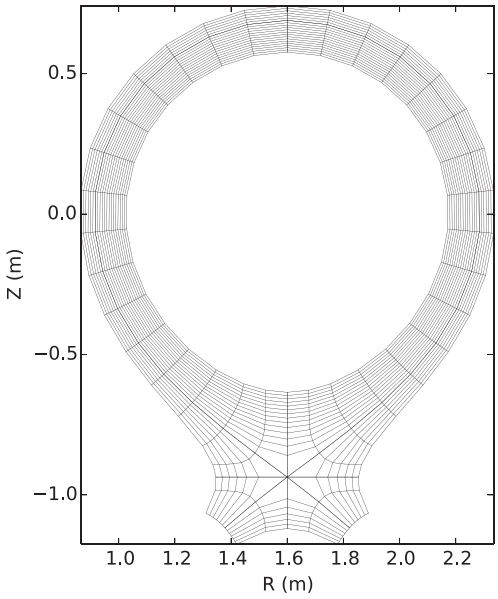

FIG. 10. A coarse version of the flux-aligned mesh in the reference poloidal plane.

$$\Psi_{CORE}(R,Z) = \frac{Ia^2L_0^2}{2q_1R_0}\log\left[q_0a^2 + q_1\left(\bar{R}^2 + Z^2/L_0^2\right)\right], \tag{37}$$

and $\bar{\Psi}(R,Z)$ is an *ad hoc* correction to generate a magnetic separatrix near the minor radius flux surface, $r = a$, given by

$$\bar{\Psi}(R,Z) = \frac{I\bar{a}_0^2L_0^2}{R_0}\log\left(0.5\sqrt{\bar{R}^2+\bar{Z}^2} + \bar{a}_1\right) \times\exp\left[-\left(\bar{R}^2+\bar{Z}^2\right)/\bar{a}_2^2\right]. \tag{38}$$

Here, $\bar{R} = (R - R_0)/L_0$, $\bar{Z} = (Z + Z_{shift})/L_0$, $R_0 = 1.6$m, $Z_{shift} = 2.0$m, $L_0 = 1.0$m, $I = RB_\phi = -3.5$Tm, $a = 0.6$, $q_0 = 1.0$, $q_1 = 2.78$, $\bar{a}_0^2 = 0.2$, $\bar{a}_1 = 0.1$, and $\bar{a}_2^2 = 1.1$. The corresponding local value of the magnetic safety factor at the outer midplane measured by $q_{loc} = (B_\phi/B_\theta)((R - R_0)/R)$ exhibits nearly linear growth from 3.4 to 4.6 across the radial extent of the simulation domain $2.17\text{m} < R < 2.34\text{m}$, and the characteristic shear value is given by $s \approx 1.2$. Details of the grid-generation in a reference poloidal plane will be reported in our future publications, while, here, we only mention that the mesh is locally orthogonal everywhere excluding regions near the block boundaries (see Fig. 10). This construction avoids extremely small poloidal cell size, which occurs near the block boundaries containing the X-point if a fully locally orthogonal grid is used.[31,45,46] For an explicit time integration scheme, such small cells can significantly restrict a stable time step determined by the Courant constraint.

The results of COGENT simulations for the case of a singly charged, $Z_i = 1$, deuterium, $m_i = 2m_p$, ion species are demonstrated in Figs. 11–14. The simulation model supports both the ITG and resistive (drift and ballooning) modes, and the present illustrative studies adopt the uniform parallel conductivity [Eq. (32)] corresponding to $\bar{\tau}_e\omega_{tr,e} = 0.37$. Here, $\omega_{tr,e} = \sqrt{T_e/m_e}/(\bar{q}R_0)$ and we take $\bar{q} = 4$.

To elucidate the structure of the ion scale turbulence in the presence of the X-point, we first consider the canonical Maxwellian initialization in Eqs. (30) and (31), which mitigates the development of large axisymmetric variations in the electrostatic potential. The corresponding initial density and temperature profiles are presented in Fig. 11, and the initial value of the electrostatic potential is set to zero. To facilitate the development of instabilities, we introduce density perturbation

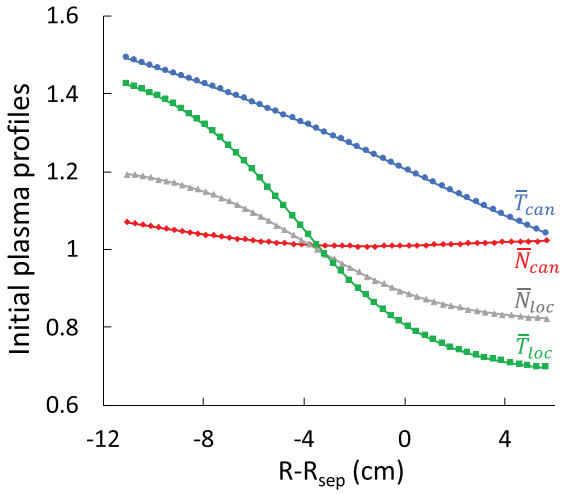

FIG. 11. Radial lineout of the initial plasma profiles at the outer midplane. Shown are the radial profiles for density (red diamonds) and temperature (blue circles) used for the simulations with the canonical Maxwellian initialization, and the radial profiles for density (gray triangles) and temperature (green squares) used for the simulations with the local Maxwellian initialization.

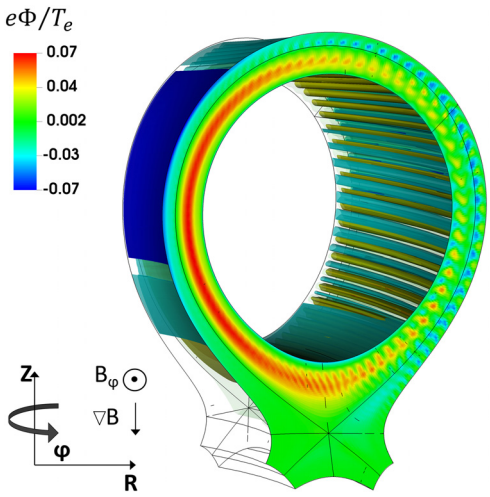

FIG. 12. Electrostatic potential variations, $e\Phi/T_e$, obtained in full-F simulations of the ion turbulence with the canonical Maxwellian initialization corresponding to $T_0 = 7$ keV. A periodic toroidal wedge of $\Delta\phi = 2\pi/16$ is considered, and the uniform value of the parallel electron conductivity corresponds to $\bar{\tau}_e\omega_{tr,e} = 0.37$. The time instance for the data shown is given by $t = 89R_0/V_{T0}$.

with an amplitude of 0.3% and toroidal and poloidal harmonic numbers of $n = 16$ and $m = 64$, respectively. The electron temperature is taken to be consistent with the characteristic value of the ion temperature, $T_e = T_0 = 7$keV. Zero radial derivatives of the electrostatic potential are adopted as boundary conditions at the inner (core) and outer (SOL) radial boundaries. A periodic toroidal wedge with $\Delta\phi = 2\pi/16$ is considered and a single toroidal block is used. The grid resolution in the poloidal plane is specified by $[N_\psi = 36,\ N_\theta = 512]$, $[N_\psi = 16,\ N_\theta = 544]$, and $[N_\psi = 16,\ N_\theta = 32]$, in the core, SOL, and private-flux regions, respectively. The number of cells in the other phase-space directions is $[N_\phi = 4, N_{v_\parallel} = 32,\ N_\mu = 24]$, and the velocity space extent is given by $-4.9V_{T0} \le v_\parallel \le 4.9V_{T0}$ and $0 \le \mu \le 10.9T_0R_0/I$, where $V_{T0} = \sqrt{T_0/m_i}$. The time step is limited by the Courant constraint for the advection operator in Eq. (1) and corresponds to $\Delta t = 0.01R_0/V_{T0}$. The simulation uses 1344 Haswell cores of the NERSC Cori cluster[47] and takes 3s of wall clock time per step.

The electrostatic potential variations during the nonlinear stage are shown in Fig. 12. Although most of the large-amplitude axisymmetric perturbations are suppressed due to the canonical Maxwellian initialization, a noticeable level of long-wavelength poloidal variations, nevertheless, remains (as seen at the inboard plane) due to poloidal variations in the initial ion density profile (see Sec. IV B for details). The short-wavelength perturbations are, however, concentrated at the outboard plane consistent with the ballooning character of the ion turbulence. Furthermore, a pronounced stabilization of the electrostatic perturbation is observed in the X-point region due to the presence of enhanced magnetic shear.

The effects of self-consistent axisymmetric electric fields characteristic of a tokamak edge are addressed in the simulations illustrated in Figs. 13 and 14 for the case where a local Maxwellian initialization is used (see Fig. 11 for the corresponding plasma profiles). More realistic values of the ion and electron temperatures are considered, $T_0 = T_e = 1.75$keV, and the effective electron collisional time in Eq. (32) is maintained at the same value of $\bar{\tau}_e\omega_{tr,e} = 0.37$. The consistent boundary condition in Eq. (15) is adopted at the inner (core) radial boundary, while the outer (SOL) radial boundary assumes a zero Neumann condition for the potential. A periodic toroidal wedge of $\Delta\phi = 2\pi/8$ is considered, and other simulation parameters including the grid resolution, velocity domain extent, and the initial density perturbation are the same as those used in the simulations with the canonical Maxwellian initialization. Figure 13 shows large-amplitude axisymmetric transient oscillations in the electrostatic potential, followed by the formation of a quasi-stationary equilibrium state with a large radial electric field. The frequency of the oscillations is found to be in a good agreement with the corresponding theoretical estimate for the geodesic acoustic mode (GAM) frequency[16,48]

$$\omega_{GAM}^2 \approx \left(\frac{7}{4} + \chi\right)\frac{2T_i}{m_iR_0^2}\left[1 + \frac{46 + 32\chi + 8\chi^2}{(7 + 4\chi)^2q^2}\right], \qquad (39)$$

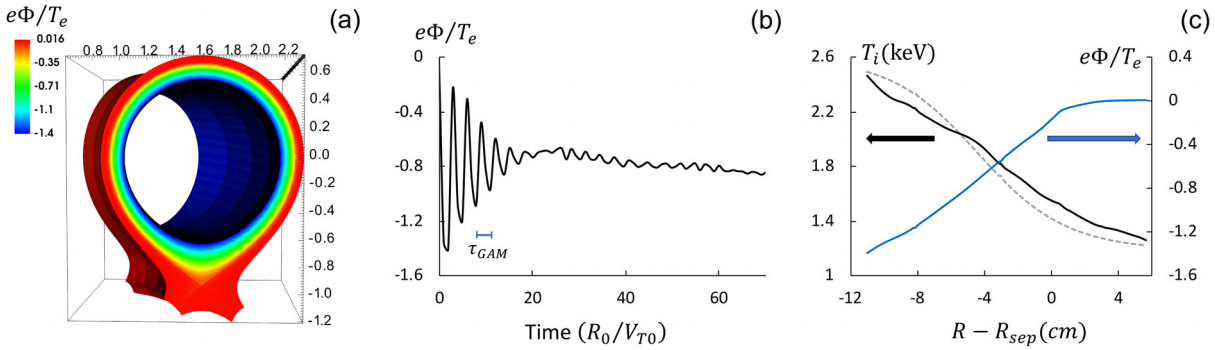

FIG. 13. Full-F simulations of the ion turbulence with the local Maxwellian initialization corresponding to $T_0 = 1.75$keV. A periodic toroidal wedge of $\Delta\phi = 2\pi/8$ is considered, and the uniform value of the parallel electron conductivity corresponds to $\bar{\tau}_e\omega_{tr,e} = 0.37$. Shown are (a) the electrostatic potential variations, $e\Phi/T_e$ at $t = 133R_0/V_{T0}$; (b) the time history of the electrostatic potential measured at the outboard midplane at $R_{sep} - R = 6.2$cm; and (c) the outboard midplane radial profiles of the ion temperature (solid black curve) and electrostatic potential (solid blue curve) at $t = 133R_0/V_{T0}$. Additionally, frame (b) illustrates the period of the GAM oscillations, $\tau_{GAM} = 2\pi/\omega_{GAM}$, where ω_{GAM} is given in Eq. (39), and frame (c) shows the initial radial ion temperature profile (dashed black curve).

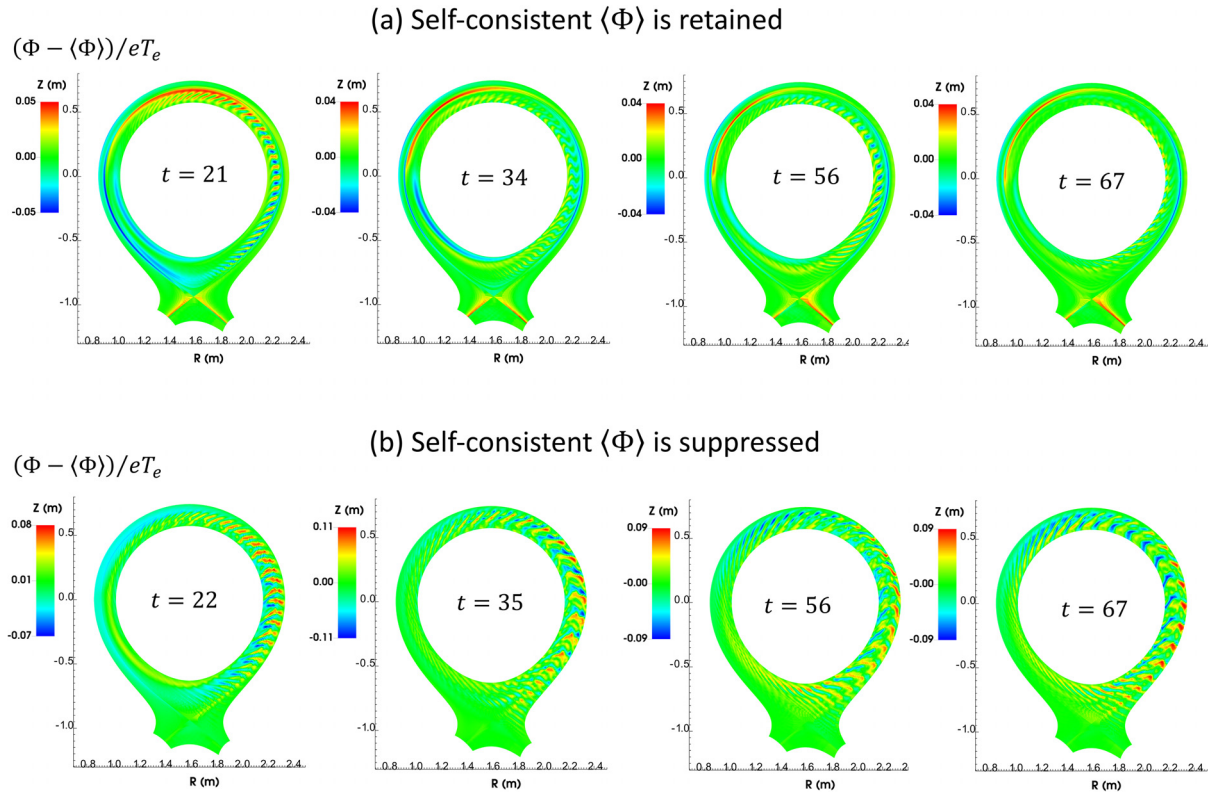

FIG. 14. Effects of the self-consistent zonal component of the electrostatic potential on the ion turbulence in a single-null geometry. The non-zonal component of the electrostatic potential, $e\tilde{\Phi}/T_e = e(\Phi - \langle\Phi\rangle)/T_e$, is shown for the cases corresponding to (a) the standard simulation model in Eqs. (1) and (18), and (b) the simulations, where the flux-surface averaged component, $\langle\Phi\rangle$, is artificially suppressed by subtracting it from the potential distribution, Φ, after each time step. The time instances illustrated in the figure are measured in the units of R_0/V_{T0}. The simulation parameters correspond to those used in Fig. 13.

where $\chi = Z_i T_e/T_i$. Taking $q = \bar{q} = 4$, $T_i = T_0$, and $\chi = 1$, we obtain $\omega_{GAM} \approx 2.4 V_{T0}/R_0$. Intermittent behavior of the ion turbulence, where the effective energy of the non-zonal component of the potential perturbation $e\tilde{\Phi}/T_e = e(\Phi - \langle\Phi\rangle)/T_e$ appears to oscillate in time, is observed in the quasi-stationary state [see Fig. 14(a)]. Such a trend is qualitatively similar to a well-known limit-cycle oscillation phenomenon; however, a more detailed analysis is required to relate the present simulation results to the existing theories[49,50] and experimental observations,[51] and will be included in later work. Here, the role of self-consistent axisymmetric potential variations is elucidated by comparing the simulations illustrated in Fig. 14(a) with those where the flux-surface averaged (zonal) component, $\langle\Phi\rangle$, is artificially suppressed by subtracting it from the potential distribution, Φ, after each time step. In the absence of a large background radial electric field (and the corresponding $E \times B$ flow shear), stronger and steady turbulence is observed [see Fig. 14(b)], thereby confirming the important role of the self-consistent axisymmetric electric fields in the regulation of edge plasma transport.

VI. CONCLUSIONS

The locally field-aligned 5D full-F finite-volume code COGENT is developed for simulations of edge plasmas in divertor geometries. The geometrical complexity related to the presence of strong magnetic shear and a magnetic X-point is handled by making use of a multiblock decomposition, in which logically distinct blocks are mapped from rectangular computational domains and are aligned with magnetic field lines to accommodate strong anisotropy induced by the magnetic field. A non-matching grid interface is allowed at toroidal block boundaries, and a high-order interpolation is used to provide inter-block coupling. The multiblock approach together with the use of a toroidal angle as a field-aligned coordinate can minimize the twist and shear of control volumes and is demonstrated to facilitate numerical simulations of plasma microturbulence in a divertor (single-null) geometry.

The COGENT code is applied to the modeling of ion-scale microturbulence in a single-null geometry. The simulation model solves the long-wavelength limit of the full-F gyrokinetic equation for ion species coupled to the quasi-neutrality (vorticity) equation for electrostatic potential variations, where an isothermal fluid approximation is adopted for an electron response. The use of the reduced vorticity model eliminates fast time scales associated with a kinetic electron response (e.g., electrostatic Alfvén wave) and provides a self-consistent description of electrostatic potential perturbations in a simulation domain that spans both open and closed field lines. Note that the standard gyrokinetic Poisson model with an adiabatic electron response

that is often used for the core plasma modeling cannot be straightforwardly extended across the separatrix. Moreover, the vorticity formulation for electrostatic potential perturbations used in COGENT explicitly includes the Reynolds stress term, which can, therefore, be turned on or off in order to assess its influence on the L-H transition process (e.g., as done in Ref. 25). This is in contrast to the gyrokinetic Vlasov–Poisson model where the effect of Reynolds stress forces is implicit, i.e., it manifests itself via the evolution of plasma species densities.

The vorticity model is verified in this work by (a) recovering the results of ITG simulations performed with the gyrokinetic-Poisson model in a toroidal annular geometry, and (b) recovering the analytical dispersion relation for the resistive drift instability in a slab geometry. A general discretization of the vorticity model is found to be prone to enhanced numerical pollution related to a highly anisotropic plasma conductivity. The pollution issue is found to strongly affect the nonlinear stage of ITG simulations, and a method to minimize the pollution effect is developed and demonstrated to work in COGENT simulations. The numerical issue is not related to the kinetic response of the ion species and is, therefore, of importance to a number of the standard computation fluid models that employ the vorticity equation. Following the aforementioned verification studies, the vorticity model is applied to cross-separatrix simulations. Magnetic-shear stabilization is observed in the X-point region, and the role of self-consistent axisymmetric potential variations is addressed. In particular, an intermittent turbulent behavior, resembling the limit-cycle oscillation phenomenon, is observed in the presence of the self-consistent axisymmetric potential variation, whereas steady and stronger turbulence appears for the case where the flux-surface average potential component is artificially suppressed in the simulations.

ACKNOWLEDGMENTS

The authors are grateful to D. Ghosh, M. Umansky, and A. Dimits for fruitful discussions. They also wish to thank their collaborators in the Applied Numerical Algorithms Group, Lawrence Berkeley National Laboratory (LBNL), for assistance in the development of the numerical algorithms and software infrastructure underlying the COGENT code. This research was supported by the U.S. Department of Energy under Contract No. DE-AC52–07NA27344.

DATA AVAILABILITY

The data that support the findings of this study are available from the corresponding author upon reasonable request.

REFERENCES

[1]J. Candy and R. Waltz, "An Eulerian gyrokinetic-maxwell solver," J. Comput. Phys. **186**, 545–581 (2003).
[2]F. Jenko, W. Dorland, M. Kotschenreuther, and B. N. Rogers, "Electron temperature gradient driven turbulence," Phys. Plasmas **7**, 1904–1910 (2000).
[3]M. Kotschenreuther, G. Rewoldt, and W. M. Tang, "Comparison of initial value and eigenvalue codes for kinetic toroidal plasma instabilities," Comput. Phys. Commun. **88**, 128–140 (1995).
[4]V. Grandgirard, J. Abiteboul, J. Bigot, T. Cartier-Michaud, N. Crouseilles, G. Dif-Pradalier, C. Ehrlacher, D. Esteve, X. Garbet, P. Ghendrih, G. Latu, M. Mehrenberger, C. Norscini, C. Passeron, F. Rozar, Y. Sarazin, E. Sonnendrücker, A. Strugarek, and D. Zarzoso, "A 5D gyrokinetic full-f global semi-Lagrangian code for flux-driven ion turbulence simulations," Comput. Phys. Commun. **207**, 35–68 (2016).
[5]Z. Lin, T. S. Hahm, W. W. Lee, W. M. Tang, and R. B. White, "Turbulent transport reduction by zonal flows: Massively parallel simulations," Science **281**, 1835–1837 (1998).
[6]E. Lanti, N. Ohana, N. Tronko, T. Hayward-Schneider, A. Bottino, B. McMillan, A. Mishchenko, A. Scheinberg, A. Biancalani, P. Angelino, S. Brunner, J. Dominski, P. Donnel, C. Gheller, R. Hatzky, A. Jocksch, S. Jolliet, Z. Lu, J. M. Collar, I. Novikau, E. Sonnendrücker, T. Vernay, and L. Villard, "Orb5: A global electromagnetic gyrokinetic code using the pic approach in toroidal geometry," Comput. Phys. Commun. **251**, 107072 (2020).
[7]J. Chowdhury, W. Wan, Y. Chen, S. E. Parker, R. J. Groebner, C. Holland, and N. T. Howard, "Study of the l-mode tokamak plasma "shortfall" with local and global nonlinear gyrokinetic δf particle-in-cell simulation," Phys. Plasmas **21**, 112503 (2014).
[8]O. V. Batishchev, S. I. Krasheninnikov, P. J. Catto, A. A. Batishcheva, D. J. Sigmar, X. Q. Xu, J. A. Byers, T. D. Rognlien, R. H. Cohen, M. M. Shoucri, and I. P. Shkarofskii, "Kinetic effects in tokamak scrape-off layer plasmas," Phys. Plasmas **4**, 1672–1680 (1997).
[9]C. S. Chang, S. Ku, G. R. Tynan, R. Hager, R. M. Churchill, I. Cziegler, M. Greenwald, A. E. Hubbard, and J. W. Hughes, "Fast low-to-high confinement mode bifurcation dynamics in a tokamak edge plasma gyrokinetic simulation," Phys. Rev. Lett. **118**, 175001 (2017).
[10]M. R. Dorr, P. Colella, M. A. Dorf, D. Ghosh, J. A. F. Hittinger, and P. O. Schwartz, "High-order discretization of a gyrokinetic Vlasov model in edge plasma geometry," J. Comput. Phys. **373**, 605–630 (2018).
[11]P. McCorquodale, M. Dorr, J. Hittinger, and P. Colella, "High-order finite-volume methods for hyperbolic conservation laws on mapped multiblock grids," J. Comput. Phys. **288**, 181–195 (2015).
[12]A. H. Hakim, N. R. Mandell, T. N. Bernard, M. Francisquez, G. W. Hammett, and E. L. Shi, "Continuum electromagnetic gyrokinetic simulations of turbulence in the tokamak scrape-off layer and laboratory devices," Phys. Plasmas **27**, 042304 (2020).
[13]Q. Pan, D. Told, E. L. Shi, G. W. Hammett, and F. Jenko, "Full-f version of gene for turbulence in open-field-line systems," Phys. Plasmas **25**, 062303 (2018).
[14]M. A. Dorf, R. H. Cohen, M. Dorr, T. Rognlien, J. Hittinger, J. Compton, P. Colella, D. Martin, and P. McCorquodale, "Simulation of neoclassical transport with the continuum gyrokinetic code COGENT," Phys. Plasmas **20**, 012513 (2013).
[15]M. A. Dorf, R. H. Cohen, M. Dorr, J. Hittinger, and T. D. Rognlien, "Progress with the COGENT Edge Kinetic Code: Implementing the Fokker-Planck Collision Operator," Contrib. Plasma Phys. **54**, 517–523 (2014).
[16]M. Dorf, R. Cohen, M. Dorr, T. Rognlien, J. Hittinger, J. Compton, P. Colella, D. Martin, and P. McCorquodale, "Numerical modelling of geodesic acoustic mode relaxation in a tokamak edge," Nucl. Fusion **53**, 063015 (2013).
[17]M. A. Dorf, M. R. Dorr, J. A. Hittinger, R. H. Cohen, and T. D. Rognlien, "Continuum kinetic modeling of the tokamak plasma edge," Phys. Plasmas **23**, 056102 (2016).
[18]M. Dorf and M. Dorr, "Continuum kinetic modelling of cross-separatrix plasma transport in a tokamak edge including self-consistent electric fields," Contrib. Plasma Phys. **58**, 434–444 (2018).
[19]M. Dorf and M. Dorr, "Progress with the 5d full-f continuum gyrokinetic code cogent," Contrib. Plasma Phys. **60**, e201900113 (2020).
[20]F. Hariri and M. Ottaviani, "A flux-coordinate independent field-aligned approach to plasma turbulence simulations," Comput. Phys. Commun. **184**, 2419–2429 (2013).
[21]J.-M. Kwon, D. Yi, X. Piao, and P. Kim, "Development of semi-Lagrangian gyrokinetic code for full-f turbulence simulation in general tokamak geometry," J. Comput. Phys. **283**, 518–540 (2015).
[22]G. Latu, M. Mehrenberger, Y. Güçlü, M. Ottaviani, and E. Sonnendrücker, "Field-aligned interpolation for semi-Lagrangian gyrokinetic simulations," J. Sci. Comput. **74**, 1601–1650 (2018).
[23]L. Ye, X. Xiao, Y. Xu, Z. Dai, and S. Wang, "Implementation of field-aligned coordinates in a semi-Lagrangian gyrokinetic code for tokamak turbulence simulation," Plasma Sci. Technol. **20**, 074008 (2018).
[24]S. I. Braginskii, "Transport Processes in a Plasma," Rev. Plasma Phys. **1**, 205 (1965).

[25]D. Galassi, G. Ciraolo, P. Tamain, H. Bufferand, P. Ghendrih, N. Nace, and E. Serre, "Tokamak edge plasma turbulence interaction with magnetic x-point in 3d global simulations," Fluids **4**, 50 (2019).
[26]F. I. Parra and P. J. Catto, "Limitations of gyrokinetics on transport time scales," Plasma Phys. Controlled Fusion **50**, 065014 (2008).
[27]F. I. Parra and P. J. Catto, "Vorticity and intrinsic ambipolarity in turbulent tokamaks," Plasma Phys. Controlled Fusion **51**, 095008 (2009).
[28]M. A. Dorf, R. H. Cohen, A. N. Simakov, and I. Joseph, "On the applicability of the standard approaches for evaluating a neoclassical radial electric field in a tokamak edge region," Phys. Plasmas **20**, 082515 (2013).
[29]Y. Idomura, "Full-f gyrokinetic simulation over a confinement time," Phys. Plasmas **21**, 022517 (2014).
[30]Y. Asahi, V. Grandgirard, Y. Idomura, X. Garbet, G. Latu, Y. Sarazin, G. Dif-Pradalier, P. Donnel, and C. Ehrlacher, "Benchmarking of flux-driven full-f gyrokinetic simulations," Phys. Plasmas **24**, 102515 (2017).
[31]T. D. Rognlien, D. D. Ryutov, N. Mattor, and G. D. Porter, "Two-dimensional electric fields and drifts near the magnetic separatrix in divertor tokamaks," Phys. Plasmas **6**, 1851–1857 (1999).
[32]M. V. Umansky, X. Q. Xu, B. Dudson, L. L. LoDestro, and J. R. Myra, "Status and verification of edge plasma turbulence code BOUT," Comput. Phys. Commun. **180**, 887–903 (2009).
[33]P. Colella, D. Graves, T. Ligocki, D. Trebotich, and B. V. Straalen, "Embedded boundary algorithms and software for partial differential equations," J. Phys.: Conf. Ser. **125**, 012084 (2008).
[34]See http://www.llnl.gov/casc/hypre/ for "hypre software library."
[35]D. Ghosh, M. Dorf, J. Hittinger, and M. Dorr, "Implicit-explicit time integration for the vlasov-fokker-planck equations," in *48th AIAA Plasmadynamics and Lasers Conference* (American Institute of Aeronautics and Astronautics, 2017).
[36]D. Ghosh, M. A. Dorf, M. R. Dorr, and J. A. F. Hittinger, "Kinetic simulation of collisional magnetized plasmas with semi-implicit time integration," arXiv:1707.08247 (2017).
[37]P. Paruta, P. Ricci, F. Riva, C. Wersal, C. Beadle, and B. Frei, "Simulation of plasma turbulence in the periphery of diverted tokamak by using the GBS code," Phys. Plasmas **25**, 112301 (2018).
[38]W. W. Lee, "Gyrokinetic particle simulation model," J. Comput. Phys. **72**, 243–269 (1987).
[39]V. Grandgirard, Y. Sarazin, X. Garbet, G. Dif-Pradalier, P. Ghendrih, N. Crouseilles, G. Latu, E. Sonnendrücker, N. Besse, and P. Bertrand, "Computing ITG turbulence with a full-f semi-Lagrangian code," Commun. Nonlinear Sci. Numer. Simul. **13**, 81–87 (2008).
[40]A. M. Dimits, G. Bateman, M. A. Beer, B. I. Cohen, W. Dorland, G. W. Hammett, C. Kim, J. E. Kinsey, M. Kotschenreuther, A. H. Kritz, L. L. Lao, J. Mandrekas, W. M. Nevins, S. E. Parker, A. J. Redd, D. E. Shumaker, R. Sydora, and J. Weiland, "Comparisons and physics basis of tokamak transport models and turbulence simulations," Phys. Plasmas **7**, 969–983 (2000).
[41]G. Merlo, J. Dominski, A. Bhattacharjee, C. S. Chang, F. Jenko, S. Ku, E. Lanti, and S. Parker, "Cross-verification of the global gyrokinetic codes GENE and XGC," Phys. Plasmas **25**, 062308 (2018).
[42]P. Helander and D. J. Sigma, *Collisional Transport in Magnetized Plasmas* (Cambridge University Press, Cambridge, 2002).
[43]M. V. Umansky, R. H. Cohen, L. L. LoDestro, and X. Q. Xu, "Suite of verification test problems for edge turbulence simulations," Contrib. Plasma Phys. **48**, 27–31 (2008).
[44]J. Hittinger and J. Banks, "Block-structured adaptive mesh refinement algorithms for vlasov simulation," J. Comput. Phys. **241**, 118–140 (2013).
[45]V. Rozhansky, S. Voskoboynikov, E. Kaveeva, D. Coster, and R. Schneider, "Simulation of tokamak edge plasma including self-consistent electric fields," Nucl. Fusion **41**, 387 (2001).
[46]V. Rozhansky, E. Kaveeva, P. Molchanov, I. Veselova, S. Voskoboynikov, D. Coster, G. Counsell, A. Kirk, S. Lisgo, ASDEX-Upgrade Team, and MAST Team, "New b2solps5.2 transport code for h-mode regimes in tokamaks," Nucl. Fusion **49**, 025007 (2009).
[47]See https://nersc.gov for "National Energy Research Scientific Computing Center."
[48]Z. Gao, K. Itoh, H. Sanuki, and J. Q. Dong, "Eigenmode analysis of geodesic acoustic modes," Phys. Plasmas **15**, 072511 (2008).
[49]E-j Kim and P. H. Diamond, "Zonal flows and transient dynamics of the $l-h$ transition," Phys. Rev. Lett. **90**, 185006 (2003).
[50]G. Y. Park, S. S. Kim, H. Jhang, P. H. Diamond, T. Rhee, and X. Q. Xu, "Flux-driven simulations of turbulence collapse," Phys. Plasmas **22**, 032505 (2015).
[51]K. Itoh, S.-I. Itoh, and A. Fujisawa, "An assessment of limit cycle oscillation dynamics prior to l-h transition," Plasma Fusion Res. **8**, 1102168 (2013).